

THESIS

AEROSOL SIZE DISTRIBUTION CHANGES IN FIREX-AQ BIOMASS BURNING
PLUMES: THE ROLE OF PLUME CONCENTRATION ON COAGULATION AND OA
CONDENSATION/EVAPORATION

Submitted by

Nicole June

Department of Atmospheric Science

In partial fulfillment of the requirements

For the Degree of Master of Science

Colorado State University

Fort Collins, Colorado

Spring 2022

Master's Committee:

Advisor: Jeffrey Pierce

Sonia Kreidenwis
Shantanu Jathar

Copyright by Nicole June 2022

All Rights Reserved

ABSTRACT

AEROSOL SIZE DISTRIBUTION CHANGES IN FIREX-AQ BIOMASS BURNING PLUMES: THE ROLE OF PLUME CONCENTRATION ON COAGULATION AND OA CONDENSATION/EVAPORATION

The evolution of organic aerosols and aerosol size distributions within smoke plumes are uncertain due to the variability in rates of coagulation and organic aerosol (OA) condensation/evaporation across different smoke plumes and potentially in different locations within a single plume. We use aircraft data from the western US portion of the FIREX-AQ campaign to evaluate differences in aerosol size distribution evolution (growing by 10s to over 100 nm in several hours), OA mass, and Oxygen to Carbon ratios (O:C) under different concentrations and amounts of dilution. The observations show diameter increasing more quickly in more concentrated plumes despite these plumes generally having more OA evaporation than in the less concentrated plumes. Initial observations of OA and O:C suggest that evaporation and/or secondary OA formation between emission and the first measurement is also influenced by plume concentration. We estimate the isolated role of coagulation on size changes using model simulations, and we estimate the role of OA condensation/evaporation on size changes using the observed time evolution of the observed OA enhancement. We find that coagulation alone explains the majority of the diameter growth in the transect averages, with more growth occurring in plumes with higher initial number and OA concentrations. Overall, for each of the smoke plumes analyzed, including OA evaporation/condensation has a relatively minor impact on the simulated diameter compared to the changes due to coagulation. Additionally, we examine

differences in evolution between the dilute and concentrated sections of the plume based on CO concentration to expand the range of plume concentrations represented in the observations. To determine if these in-plume concentration gradients could be used to understand smoke plumes outside of the range of the sampled average concentration, we simulate the dilute and concentrated plume regions independently (no mixing). In these simulations of each smoke plume region, the model underestimates particle growth in the less-concentrated regions of the plume and overestimates particle growth in the more-concentrated regions. This poor comparison suggests that turbulent mixing between the more- and less-concentrated regions is occurring on timescales too fast for the regions to evolve independently, but slow enough that aerosol size differences are still seen between the regions. The mixing in the plume limits the ability for our conclusions on variations in growth and condensation/evaporation within a plume to be applied to other plumes of a similar concentration. Overall, we conclude that coagulation dominates growth with plume concentrations being important in determining how much coagulative growth is observed.

ACKNOWLEDGMENTS

I would like to thank my advisor Jeffrey Pierce, as well as my committee for their support in this work. I would also like to thank the co-contributors who collected the data and/or provided insights into the analysis: Anna Hodshire, Elizabeth Wiggins, Edward L. Winstead, Claire E. Robinson, K. Lee Thornhill, Kevin J. Sanchez, Richard Moore, Demetrios Pagonis, Hongyu Guo, Pedro Campuzano-Jost, Jose L. Jimenez, Matthew Coggon, and Matthew Alvarado. This work will be submitted to a peer-review journal. We also acknowledge the entire FIREX-AQ science team for their efforts in creating the dataset used in this work. This work is supported by the U.S. National Science Foundation.

TABLE OF CONTENTS

ABSTRACT	ii
ACKNOWLEDGEMENTS	iii
Chapter 1 Introduction	1
Chapter 2 Methods	8
2.1 DC8 Aircraft Observations	8
2.2 Coagulation Model	16
Chapter 3 Results	19
3.1 Observations	19
3.2 Estimating Drivers of Observed Growth	28
Chapter 4 Conclusions	36
References	38
Appendices	46
Appendix A Supplementary Tables	46
Appendix B Supplementary Figures.....	48

Chapter 1

Introduction

Open biomass burning (landscape fires, including wildfires) is a significant source of aerosols and vapors in the atmosphere (Akagi et al., 2011; Gilman et al., 2015; Hatch et al., 2015; Jen et al., 2019; Reid et al., 2005; Yokelson et al., 2009). Aerosol particles emitted through biomass burning are mainly composed of organic aerosol (OA) (often >90%) along with some black carbon (BC) with inorganic species (Bond et al., 2013; Capes et al., 2008; Carrico et al., 2008; Cubison et al., 2011; Hecobian et al., 2011; Mardi et al., 2018; Reid et al., 2005). These aerosol particles impact the health and welfare of communities exposed to the smoke as well as affect the Earth's radiative budget and climate (Carrico et al., 2008; Ford et al., 2018; Gan et al., 2017; Liu et al., 2015; O'Dell et al., 2019; Petters et al., 2009; Ramnarine et al., 2019; Reid et al., 2016; Shrivastava et al., 2017). Regarding these radiative/climate effects, the smoke particles have a direct radiative effect by scattering/absorbing solar radiation (Alonso-Blanco et al., 2014; Charlson et al., 1991; Haywood and Boucher, 2000; Jacobson, 2001; Ramnarine et al., 2019). As well, the aerosols have an indirect aerosol effect on climate through acting as cloud condensation nuclei (CCN) modifying the cloud albedo and lifetime (Albrecht, 1989; Lee et al., 2013; Pierce and Adams, 2007; Ramnarine et al., 2019; Spracklen et al., 2011; Twomey, 1974).

Particle size influences the degree to which the aerosols impact health and the magnitude of the direct and indirect radiative effects (Kodros et al., 2018; Lee et al., 2013; Seinfeld and Pandis, 2016; Spracklen et al., 2011). Particulate matter is deposited into different locations in the respiratory tract based on particle size (Hinds, 1999; Kodros et al., 2018), and the toxicity of particulate matter from wildfires has also been linked to particle size (Jalava et al., 2006;

Johnston et al., 2019; Leonard et al., 2007). The absorption/scattering efficiencies of the aerosols is determined by their size and composition (Seinfeld and Pandis, 2016). The scattering and Angstrom exponent of biomass burning are correlated with smoke age as a result of their dependence on aerosol size (Junghenn Noyes et al., 2020; Kleinman et al., 2020). The ability of aerosols to act as CCN and then impact cloud properties is determined by the particle diameter and hygroscopicity (Lee et al., 2013; Petters and Kreidenweis, 2007; Spracklen et al., 2011). Lee et al. (2013) found that CCN concentrations were highly sensitive to uncertainties in biomass burning diameter, and Ramnarine et al. (2019) showed both the aerosol indirect effect and the direct radiative effect of biomass burning were sensitive to the aerosol size. Therefore, to accurately determine the climate and health effects of biomass burning aerosols, the particle size must be well understood.

Aerosol size distributions from biomass burning evolve after emission with size distributions tending to shift to larger sizes and have a decrease in modal width due to condensation/evaporation and coagulation (Hodshire et al., 2019b, 2021; Janhäll et al., 2010; Levin et al., 2010; Sakamoto et al., 2016). Janhäll et al. (2010) showed that fresh smoke (< 1 hour) had median diameters ranging from 100 nm to 150 nm with modal widths varying between 1.6 and 1.9, while aged smoke (several hours to several days) had larger median diameters ranging from 200 nm to 300 nm with modal widths of 1.3 to 1.6. The Biomass Burning Observation Project (BBOP) campaign observed particle diameters to statistically increase with aging with smoke sampled ~15 minutes after emission having median diameters of 40 nm to 150 nm, and smoke with an age of ~3 hours having median diameters of 175 nm to 260 nm (Hodshire et al., 2021). Observations of regional haze dominated by smoke over Brazil were also observed to have an increase in particle diameter (120 nm to 180 nm) and a decrease in modal

width (1.73 to 1.63) as it aged (Reid et al., 1998). Past modeling work has shown the size distribution changes observed in biomass burning plumes are due to both condensation/evaporation and coagulation (Hodshire et al., 2019b; Sakamoto et al., 2016). Both of these studies estimated that coagulation had the largest effect on diameter changes at high concentrations with slow dilution rates. In Hodshire et al. (2019b), the simulated diameter change due to both condensation and coagulation seen in four hours ranged from 10 nm in dilute plumes to 125 nm in concentrated plumes.

Coagulation reduces particle number, shifts the distribution to larger sizes, and narrows the modal width of the size distribution (Hodshire et al., 2019b; Janhäll et al., 2010; Sakamoto et al., 2016; Seinfeld and Pandis, 2016). The coagulation rate is proportional to the square of the number concentration, meaning that more concentrated smoke plumes have more rapid growth due to coagulation. Hence, the initial concentrations in the plume affects the coagulation rate; and because dilution of clean, background air into smoke plumes lowers number concentrations, the plume dilution rate also impacts the coagulation rate (Sakamoto et al., 2016). Importantly, most chemical transport and climate models are too coarse to resolve individual plumes and their dilution. In these models, the emissions are instantly diluted through the course gridboxes, thus underestimating the role of coagulation. To remedy this, Sakamoto et al. (2016) developed a parameterization of coagulation within sub-grid-scale diluting smoke plumes. Ramnarine et al. (2019) used this sub-grid parameterization of biomass burning and found that representing this in-plume coagulation impacts the radiative effect of biomass burning, changing the direct radiative effect by up to 22% and the indirect effect by up to 43%, underscoring the importance of near-source, sub-grid coagulation in shaping the aerosol size distribution and radiative effects.

Organic aerosol (OA) condensation/evaporation can also lead to growth/shrinkage of the median diameter (Hodshire et al., 2019b; Riipinen et al., 2011; Zhang et al., 2012). If there is secondary organic aerosol (SOA) formation in the smoke plume, this SOA can condense onto existing particles leading to growth of the size distribution; this has been suggested by lab studies of biomass burning aerosol and in past field campaigns (Bian et al., 2017; Cubison et al., 2011; Hodshire et al., 2019b; Reid et al., 1998; Yokelson et al., 2009). A substantial fraction of primary organic aerosol (POA) in biomass burning plumes is semi-volatile, allowing for evaporation of POA from particles as the plume dilutes, and cleaner air is entrained into the plume (Bian et al., 2017; Cubison et al., 2011; Huffman et al., 2009; Jolleys et al., 2015; May et al., 2015, 2013). Hence, similar to coagulation, the initial concentration and dilution rate influences the evaporation of POA in the plume. This evaporation acts to decrease particle size. The net change in OA in the smoke plume determines the overall impact of OA condensation/evaporation on the aerosol size.

Field observations have shown that OA enhancement ratios can increase, decrease, or remain constant in the first 24 h of physical smoke aging (Akagi et al., 2012; Hecobian et al., 2011; Hobbs et al., 2003; Jolleys et al., 2015; May et al., 2015; Sakamoto et al., 2015; Vakkari et al., 2014; Yokelson et al., 2009; Zhou et al., 2017). OA enhancement ratios are the in-plume OA with the background (out-of-plume) concentration of OA removed (that is, the “background corrected” OA) normalized by an inert species, typically background corrected CO (Akagi et al., 2012); OA enhancement ratios correct for dilution, and show the net change in OA as the smoke ages. Some prior works suggest SOA condensation and POA evaporation are simultaneously occurring in smoke plumes with the balance between the two determining how net OA changes (Bian et al., 2017; Hodshire et al., 2019b, a; May et al., 2015; Palm et al., 2020). Akherati et al.

(2022) performed OA simulations of wildfire plumes measured during the WE-CAN field campaign, which support this condensation-evaporation balancing hypotheses, showing that dilution-driven evaporation of POA and simultaneous production of SOA explains the lack of change in OA enhancement ratios often observed in field campaigns. Theoretical work has shown that OA enhancement ratio and composition changes may also be related to plume concentration (Bian et al., 2017; Hodshire et al., 2019b). However, Hodshire et al. (2021) showed with BBOP data no statistically significant relationship between OA changes and smoke age or initial plume concentration.

As the smoke plume ages, OA also undergoes changes in composition. Oxygen to Carbon (O:C) elemental ratios of OA can be used as a tracer for oxidative aging and SOA in the smoke plumes. Field and lab campaigns have shown that O:C typically increases as the smoke plume ages (DeCarlo et al., 2008; Hodshire et al., 2019a, 2021). The O:C increases observed in smoke plumes help to explain the no observed net change in OA, the SOA has a higher O:C than the POA, so as SOA increases and POA decreases, O:C increases (Akherati et al., 2022, Hodshire et al., 2021, 2019a). In BBOP and WE-CAN, O:C increases were inversely related to OA concentrations measured at the first transects (Akherati et al., 2022, Hodshire et al., 2021). Often these first transects are at 15-30 minutes of smoke age, so OA enhancement ratio and O:C changes occurring prior to the first transect (due to SOA formation and POA evaporation) may also be important (Hodshire et al., 2019a). Therefore, since dilution to low concentrations drives the POA evaporation, plumes with lower concentrations at the first transect may have higher O:C and a lower OA enhancement ratio at the time of the first transect (Akherati et al., 2022).

As described above, the plume concentrations (and subsequent dilution) influence the evolution of the smoke plume, including coagulation and OA evaporation/condensation rates;

plume concentrations and dilution rates span orders of magnitude with plume size. Dilution rates in smoke plumes vary with plume size and atmospheric stability. Under the same atmospheric stability conditions, a larger plume will dilute more slowly than a smaller plume since it will take longer for the background air to mix into the core of the plume (Bian et al., 2017; Hodshire et al., 2019b). The variability in plume size can lead to differences in dilution and therefore also size, number, and OA at the time of the first measurement, as well as influence the observed coagulation and OA evaporation/condensation. Since fires range in size, it is important to consider the plume concentrations in studies working to understand plume aging; however, studies using field work to determine this relationship are limited.

In addition to concentrations and dilution rates varying due to plume size, concentrations also vary based on the radial position in the smoke plume (Decker et al., 2021; Hodshire et al., 2021; Peng et al., 2020), leading to differences in coagulation and OA evaporation/condensation between the edge and core of a plume (Hodshire et al., 2021). Although fires span orders of magnitude in size with a large number of fires burning an area less than 0.1 km², field campaigns tend to sample fires this size and larger (Hodshire et al., 2019a). However, we may be able to segregate sampled plumes into relatively concentrated and dilute sections to gain a better understanding of how smaller undersampled plumes may evolve, based on the evolution of the less-concentrated plume edges (Hodshire et al., 2021). Hodshire et al, (2021) used this method to examine the relationship of the following individual variables with initial OA mass concentration and physical smoke age using the BBOP campaign: OA mass, OA oxidation state, aerosol diameter, and aerosol number concentration. The analyzed smoke plumes did show differences in plume edge and core evolution, with evidence of O:C changes occurring rapidly prior to the first transect in less concentrated plumes and plume edges, and a correlation of diameter with plume

age and concentration (Hodshire et al., 2021). However, the Hodshire et al. (2021) study did not consider mixing between radial portions of the plume within the smoke plume in their analysis, implicitly assuming that each more and less concentrated region evolved independently; and they noted the need for improvement in understanding O:C and particle diameter changes based on initial plume concentrations as well as fuel type (Hodshire et al., 2021).

In this work, we use the observations of plumes in the western US during the FIREX-AQ campaign to examine the role of plume concentration on variability in aerosol size and OA evolution between and within smoke plumes. Further, we evaluate the roles of coagulation and condensation/evaporation in the aerosol size changes. To help elucidate the role of plume concentration on biomass burning aerosol size and OA evolution, we analyze the evolution of both transect-averaged smoke aerosol properties as well as the differences between the dilute and concentrated portions of the smoke plume. We use an aerosol-microphysics model to estimate how much of the aerosol size changes growth is due to coagulation versus OA condensation/evaporation. Finally, we investigate the timescale of mixing between the more and less concentrated regions of plumes to determine if aging in these portions of the plumes can be assumed to occur independently. In Chapter 2, we describe our methods. In Chapter 3, we first present our results based on the FIREX-AQ observations, then we present our results estimating the aerosol size changes due to coagulation and condensation/evaporation. We summarize our conclusions in Chapter 4.

Chapter 2

Methods

2.1 DC8 Aircraft Observation Data

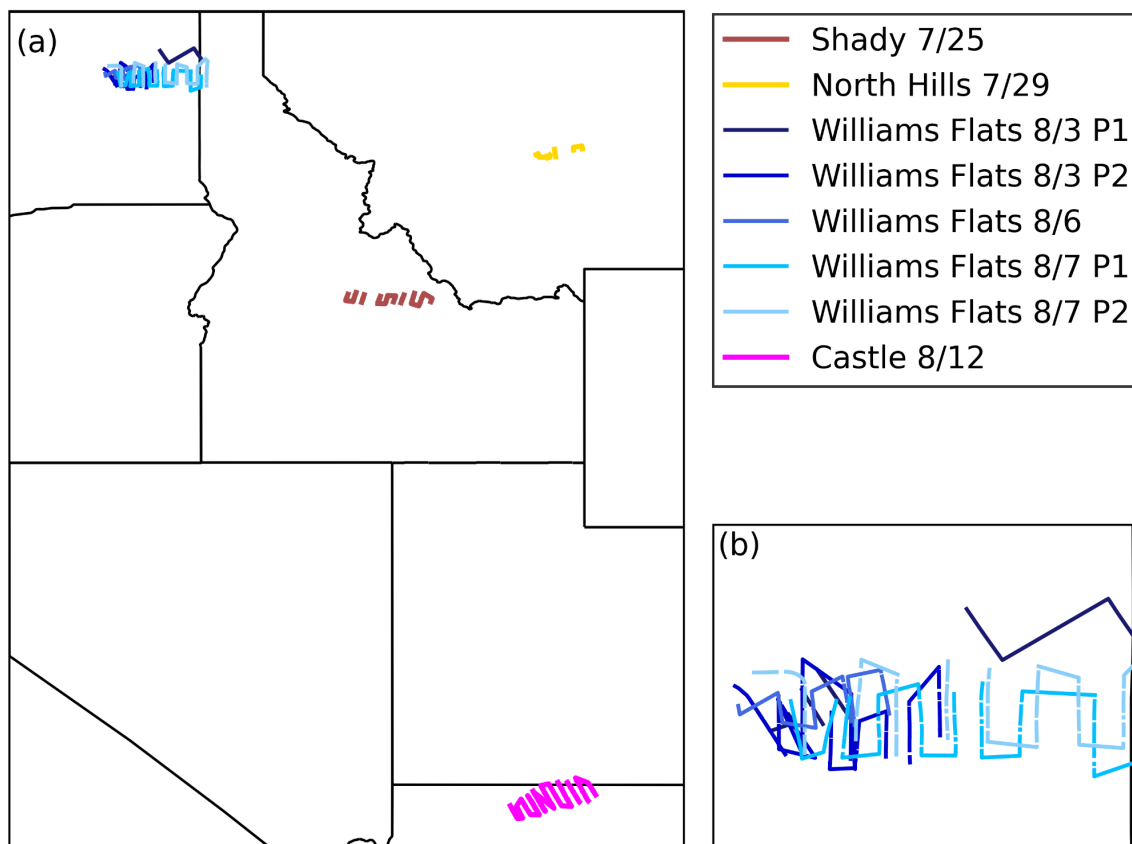


Figure 2.1: (a) Map of in-plume sections for the eight sets of transects used in this study from the FIREX-AQ campaign between July 25 and August 12, 2019. (b) Map of the in-plume sections of the five sets of transects of the Williams Flats fire.

The FIREX-AQ campaign took place in July-August 2019, sampling wildfire smoke in the Western US and agricultural smoke in the Southeastern US (<https://www-air.larc.nasa.gov/missions/firex-aq/>). In our study, we use eight sets of pseudo-Lagrangian transects from the Western United States (Figure 2.1), where the DC8 aircraft crossed the plume repeatedly, generally moving from close to the fire to further from the fire. Samples from the Southeastern portion of the campaign were not used since this portion of the

campaign had a limited number of pseudo-Lagrangian transects. The eight sets of pseudo-Lagrangian transects are from four different fires on six days. The Williams Flats fire was sampled twice on two of the days. The fuels burned varied between fires as well as between the different sampling days of the Williams Flats fire (Table 2.1). Although a true Lagrangian sampling (sampling the same air repeatedly over time as it moves downwind of the fire) is best for isolating the processes influencing aerosol aging, the DC8 aircraft generally flew downwind at two to four times the wind speed at the sampling altitude (Figure A.1), meaning that the smoke sampled farther from the fire had generally been emitted by the fire earlier in the day than the smoke sampled close to the fire. As a baseline test for the consistency in smoke emissions across the times where the sampled smoke was emitted, we excluded additional plume samplings from the western portion of the campaign due to those plumes having a non-zero-slope ($p < 0.05$) linear relationship between modified combustion efficiency (MCE) and plume age. Additionally, the Williams Flats fire plume sampling on August 8th was excluded due to non-pseudo-lagrangian sampling. More details on how we select and modify plume samplings are given in Chapter 2.1.3. However, we expect that the deviation from perfectly Lagrangian sampling in the remaining sets of transects may still influence our results, and we discuss the implications of this potential influence throughout.

Table 2.1: Information on the Fires

Flight Date	Fire	Number of sets of pseudo-lagrangian transects	Fuel	Flight Time vs Smoke Age Slope
7/25/2019	Shady	1	Timber, Shrubs/Brush, Grass	2.15
7/29/2019	North Hills	1	Timber, Shrubs/Brush, Grass	2.55
8/3/2019	Williams Flats	2	Grass	3.97, 2.34
8/6/2019	Williams Flats	1	Timber, Grass	2.88
8/7/2019	Williams Flats	2	Timber, Grass, Brush	2.96, 2.94
8/12/2019	Castle	1	Grass, Timber	3.16

2.1.1 Aircraft Instruments

The TSI laser aerosol spectrometer (LAS) measured the particle size distribution between 0.1 and 5 μm at 1 Hz resolution; these measurements have been corrected for saturation and evaporation. The LAS uses a helium-neon gas laser with the ability to detect particles as small as 90 nm in diameter and as large as 7.5 μm with 20% uncertainty across all sizes. The LAS was calibrated using size-classified ammonium sulfate aerosols (refractive index of 1.52 +0i) (Moore et al. 2021). We apply corrections to the LAS measurements for both evaporation due to heating in the sampling lines and optical saturation of the LAS sensor. Regarding saturation of the LAS measurements, we use work from Nault et al. (2018) that we linearly extrapolate to higher aerosol number concentrations (from $2 \times 10^3 \text{ cm}^{-3}$ to $2.3 \times 10^5 \text{ cm}^{-3}$) to correct for this saturation. Although it is well known that the LAS saturates at high concentrations, the functional dependence of this is unknown; therefore, there are some uncertainties introduced by assuming a

linear dependence (Figure A.2), and we investigate this by examining the differences in our model simulations of median diameter when using a linearly extrapolated correction, a quadratically extrapolated correction, or no saturation correction. In FIREX-AQ, the LAS also operated with a dilution system, and this dilution is corrected prior to saturation correcting the measurements. Next, we apply an evaporation correction for evaporation in the inlet tube due to temperature differences with the ambient air; evaporation due to the dilution system is believed to be minor and is not included. The evaporation correction is applied to the median particle diameters calculated from these size distributions based on calculations of what the mass fraction remaining (MFR). The MFR is unique for each flight based on the ambient and inlet temperatures, and OA concentration; in the flights used in our analysis the ambient and inlet temperatures were typically 273 K and 300 K, respectively (Pagonis et al. 2021). We assume that the fractional change in diameter from the evaporation correction is size independent and is found from the following equation:

$$D_p = D_{p,measured} \left(\frac{1}{MFR} \right)^{1/3} \quad (2.1)$$

Figure A.3a shows this evaporation correction for OA concentrations $1 \mu\text{g m}^{-3}$ to $2000 \mu\text{g m}^{-3}$ assuming a particle diameter of 300 nm for an ambient temperature of 273 K, inlet temperature of 300 K, and a pressure of 700 mb. Figure A.3b and A.3c show the impact on MFR and the diameter correction for an OA concentration of $1000 \mu\text{g m}^{-3}$. To test the sensitivity of our results to the assumption that the evaporation occurring in the inlet tubes is independent of size, we use the slope of Figure A,3b and the MFR for a diameter of 300 nm at $1000 \mu\text{g m}^{-3}$ to create a size-dependent evaporation correction.

The Aerodyne high-resolution time-of-flight aerosol mass spectrometer (AMS) measured OA. The AMS operated in fast spectrum mode to provide data at 1 Hz resolution. The uncertainty for the AMS measured organics was +/- 38% due to uncertainties in ionization efficiency (IE). The relative ionization efficiency for OA was calibrated pre-campaign in the laboratory (Pagonis et al. 2021, Guo et al. 2021) and assumed to be constant in the observations. We also applied the Pagonis et al., (2021) evaporation correction to the AMS data. However, the inlet residence time for the AMS was much shorter than that of the LAS, so the AMS MFR is generally much closer to 1 than that of the LAS (less correction for the AMS).

Regarding other DC-8 instruments used in this study, CO was measured by the NOAA LGR at 1 Hz resolution. The instrument operated with 2% uncertainty during the FIREX-AQ campaign. The meteorological measurement system (MMS) provides measurements of the 3D wind field, temperature, and turbulent dissipation rate. For the MMS we used 20 Hz measurements, instead of 1 Hz, to have a higher temporal resolution for calculating mixing parameters.

2.1.2 Derived Parameters from Observations

The FIREX-AQ dataset provides background flags used for determining the background concentrations of species. Each fire sampled has a fire-ID in the dataset, which indicates when the DC-8 was sampling in a plume. The background concentrations for CO for the transects used in our analysis ranged from 76 to 166 ppb, with the minimum in plume CO concentrations ranging from 98 to 300 ppb. The smoke age was provided in the dataset based on the aircraft-measured wind speeds and straight line horizontal advection between the fire and aircraft position.

The concentration enhancement of species X due to the presence of smoke (ΔX) is determined by subtracting the average background concentration of this species from the in-plume measurements. We correct for dilution by creating an enhancement ratio (sometimes referred to as a normalized excess mixing ratio, NEMR; Akagi et al. (2012)). These enhancement ratios are found by normalizing the background-corrected species (ΔX) by background-corrected CO (ΔCO), since CO is inert on timescales of near-field aging (Yokelson et al., 2009)

$$\frac{\Delta X}{\Delta CO} = \frac{X_{inplume} - X_{background}}{CO_{inplume} - CO_{background}} \quad (2.2)$$

Increases or decreases in this enhancement ratio ($\Delta X/\Delta CO$) indicate production or removal of that species in the smoke plume (provided that the sampling is close-enough to Lagrangian that variability in emissions do not impact changes in the observed enhancement ratios). In this study we look at $\Delta N/\Delta CO$ (number enhancement ratio), and $\Delta OA/\Delta CO$ (organic aerosol enhancement ratio, referred to as OAER).

Following Hodshire et al. (2021), mass concentrations of O and C are calculated using the AMS measurements of the O/C and H/C ratios. We assume that all OA mass is from O, H, and C, allowing us to calculate background-corrected O/C using the following equation:

$$\frac{\Delta O}{\Delta C} = \frac{(O_{inplume} - O_{background})}{(C_{inplume} - C_{background})} \quad (2.3)$$

The median diameter (D_p), number concentration (N) and modal width of the size distribution (σ) are calculated by fitting a lognormal distribution to the binned $dN/d\log D_p$ measurements from the LAS. N is the number concentration between 50 nm and 800 nm, the range of diameters used to fit the $dN/d\log D_p$ measurements. We examine the change in number enhancement ratio within this size range.

For each of the variables described above: D_p , $\Delta N/\Delta CO$ (number enhancement ratio), OAER, $\Delta O:\Delta C$, an ordinary least squares regression is used to calculate its rate of change as the smoke ages. For each variable, the 95% confidence interval of the regression varies between sets of transects. Due to these varying uncertainties, a Monte Carlo method was used to determine the influence of initial OA concentration (ΔOA_i) on the evolution of these variables. For example, to determine the relationship between the rate of change of D_p (dD_p/dt) and ΔOA_i ; 1000 iterations of a linear regression were performed while varying the dD_p/dt for each individual set of within its 95% confidence interval from the linear regression. The 95% confidence interval for the relationship between dD_p/dt and ΔOA_i is determined based on the 2.5 and 97.5 percentile of the slopes from the Monte Carlo linear regressions. We also perform the linear regressions assuming dD_p/dt to be the center of the 95% confidence interval, while sequentially removing one set of transects at a time. The Monte Carlo and the removing one set at a time methods of fitting help to visualize and quantify the uncertainties of the relationship between the rate of change of each of our variables of interest and ΔOA_i .

In addition to utilizing transect-average values, to investigate if high and low concentrated portions of the plumes evolve differently, we divide each transect into ΔCO percentiles to evaluate the dilute and concentrated portions of the smoke plume separately. The percentiles used are 5 to 15, 15 to 50, 50 to 90, and 90 to 100. The lowest percentile bin starts at the 5th percentile to provide a buffer between the background and in plume. Figure A.4 shows the locations of the percentiles in each of the eight plumes used in this analysis. We note that the spatial distribution of these percentiles within each smoke plume is complex, with the most concentrated percentiles not always falling in the physical center of the plume.

The ability to gain insight into the differences in processes/aging between the dilute and concentrated portions of the same plumes may be limited if mixing between our CO-percentile regions is occurring on timescales faster than several hours (the aging time observed by the aircraft). We use the following procedure to estimate the timescale of this mixing within each plume. (1) The mean and standard deviations of each wind component are calculated using an averaging time approximately equal to the length of time the DC8 spends sampling a plume transect. (2) The standard deviations of the North-South wind (σ_v) and vertical wind (σ_w) and the mean East-West wind (\bar{u}) are used to approximate the lateral ($\sigma_\theta = \sigma_v/\bar{u}$) and vertical ($\sigma_\phi = \sigma_w/\bar{u}$) turbulence intensities. (3) The Pasquill stability class (Arya, 1999) is estimated using these turbulence intensities (Table A.1). (4) Gaussian dispersion relations are used to calculate a turbulent diffusivity, from which a mixing length is determined (Seinfeld and Pandis, 2016). (5) The distance and mixing time between the 5 to 15 percentile bin and the 90 to 100 percentile bin is calculated by using the geographic coordinates of the innermost point in the 5 to 15 percentile bin, and the average geographic coordinates of the 90 to 100 percentile bin. (6) The mixing length and distance between the percentiles is used to determine the mixing time.

2.1.3 Identification of useable transects

MCE trends were checked to determine which of the flights from the western half of the campaign have sufficiently constant ratios of CO and CO₂; the eight flights used in our analysis do not have a statistically significant trend (p-value less than 0.05) in MCE with smoke age (Figure A.5). Additionally, the selected flights have the evaporation correction available, so we are able to apply both the saturation and evaporation correction to all samplings analyzed.

For the first set of transects of the Williams Flats fire on 8/3 (Williams Flats 8/3 P1 on figures), transects are limited to those that are to be most Lagrangian as identified in Wang et al. (2021). These were determined based on locations within the plume vertically based on the LIDAR measurements. The transects not used in our analysis were towards the top of the plume, while the transects used in our analysis are vertically in the densest section of the plume (Wang et al., 2021).

The transect used to initialize the coagulation model (Chapter 2.2) is not the youngest smoke sampled in 6 cases (Table A.2). Williams Flats 8/3 P1 is not initialized with the youngest smoke sampled due to the use of the Lagrangian transects as detailed above. For the seven other samplings, the $\ln(\Delta\text{CO})$ with smoke age in combination with the altitude of the plane is used to determine if the first transect should be modified. As the plume dilutes, the $\ln(\Delta\text{CO})$ should linearly decrease with smoke age, therefore the youngest transect should have the highest $\ln(\Delta\text{CO})$. If this is not the case, then we remove the closest transect from our analysis, since it is possible that transect was vertically in a different section of the plume or burn conditions at that time differed from the subsequent transects. Specific details for the transect selected to initialize the model are in Table A.2.

2.2 Coagulation Model

We use an aerosol microphysics box model to simulate the change in the aerosol size distribution due to coagulation and dilution in the smoke plumes. The model is initialized using the median diameter, total number concentration, and the modal width of each smoke plume or ΔCO percentile based on a lognormal fit of the observed values at the first transect. The model is run seven and a half hours forward in time. The aerosol size distribution is represented with 300

logarithmically spaced, single-moment size bins between 50 and 800 nm, going up to a larger maximum diameter (2 μm) did not affect the results enough to change our conclusions. We assume that the particles have a density of 1400 kg m^{-3} . The model simulates Brownian coagulation using the Fuchs form of the Brownian coagulation kernel (Fuchs, 1964).

For each set of transects, dilution is included in the model by using observed first-order decay rate of ΔCO . The dilution factor (k_{dil}) is used to calculate the rate of number change due to dilution in each size bin:

$$\left(\frac{dN}{dt}\right)_{\text{dil}} = - N_{\text{bin}} k_{\text{dil}} \quad (2.4)$$

In the base simulations of this model, the aerosol size distribution is changed at each time step only through the combined effects of dilution and coagulation.

We show additional results, where the evaporation and/or condensation of organic aerosol are also taken into account by using the observed linear fits of the $\Delta\text{OA}/\Delta\text{CO}$ ratio with smoke age for each set of transects. In this calculation, we assume that there is no new-particle formation, so all SOA condenses onto existing particles. The fractional change in OA is assumed to be constant across all sizes such that the fractional change in diameter is the same for all sizes. We assume that the evaporation and condensation does not impact the coagulation rates. For small changes due to condensation/evaporation, the change in the modal width is small and it should not have a significant impact on the coagulation rate. For example, if there is less than a factor 2 change in OA mass, there would be a small change in modal width and the change in the coagulation rate of less than 10% (Sakamoto et al., 2016; Seinfeld and Pandis, 2016). As we show in the results, the uncertainty due to these assumptions is smaller than the uncertainties in the measurements (e.g., saturation and evaporation corrections). The modeled diameter with the OA production/loss is included using the following equation:

$$D_{pm,wOA} = D_{pm,coag} \left(\left(\frac{d(\Delta OA/\Delta CO)}{dt} t \right) + 1 \right)^{1/3} \quad (2.5)$$

where $D_{pm,coag}$ is the simulated diameter at each time step considering only coagulation and dilution, $\frac{d(\Delta OA/\Delta CO)}{dt}$ is the observed change in the OA enhancement ratio with time, and t is the simulation time.

Chapter 3

Results

3.1 Observations

On average, D_p increases more rapidly in the more concentrated smoke plumes, both for the transect averages and the ΔCO percentiles (Figure 3.1). As seen in Figure A.6, some flights have a more consistent increase in D_p with smoke age than others. For example, North Hills 7/29 and Williams Flats 8/7 P2 have a constant increase in D_p with smoke age with very little noise from one transect to the next, this gives the slope of their fits a small uncertainty range, compared to a day with more variability in D_p from transect to transect such as Williams Flats 8/6. Using the Monte Carlo fitting method to consider these uncertainty ranges, the rate of change of D_p with smoke age (dD_p/dt) increases by $4.3 \text{ nm hr}^{-1} \log(\mu\text{g m}^{-3})^{-1}$ with the 95% confidence intervals in Table 3.1. Grouping by ΔCO percentile allows each plume set to span a wider range of concentrations (albeit, mixing between percentiles may influence these trends, which will be explored later), the relationship between D_p increase and plume concentration is strengthened, as seen by the reduction in the size of the 95% confidence bounds from the transect average statistics. With the ΔCO percentiles, the Monte Carlo fitting has an average slope of $3.9 \text{ nm hr}^{-1} \log(\mu\text{g m}^{-3})^{-1}$ (Table 3.1). The Pearson correlation coefficient of dD_p/dt and ΔOA_i is 0.53 and 0.43 for the transect averages and ΔCO percentiles, respectively. Based on these categories for a correlation coefficient: 0.0-0.19 is very weak, 0.2-0.39 is weak, 0.4-0.59 is moderate, 0.6-0.79 is strong and 0.8 to 1.0 is very strong (Evans, 1996), there is a moderate relationship between dD_p/dt and ΔOA_i . Similarly, the BBOP campaign showed moderate correlation between D_p and smoke age (Hodshire et al., 2021). The growth shown in Figures 3.1 and A.6 is a combined impact of coagulation, net condensation/evaporation, and noise and trends due to the

influence of parcel changes due to imperfect Lagrangian sampling; in Chapter 3.2 we attempt to quantify how much of the diameter change is due to coagulation, or condensation/evaporation.

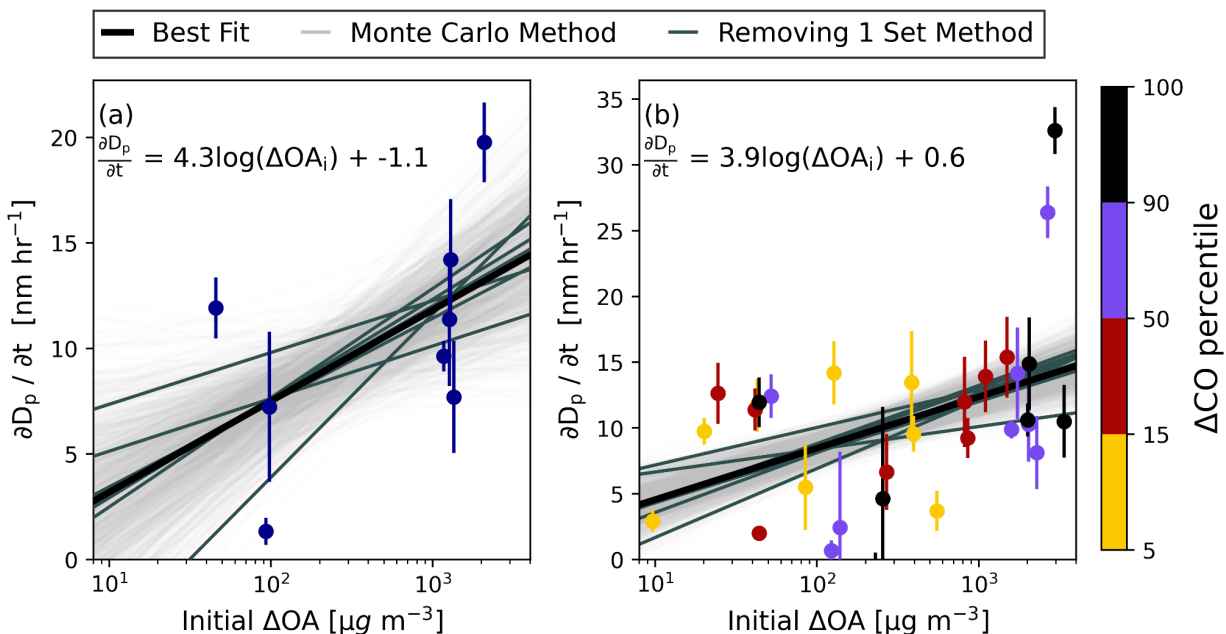


Figure 3.1: Observed slopes of median diameter with smoke age based on ordinary least squares linear regressions (dD_p/dt) as a function of ΔOA_i (initial background-corrected organic aerosol) for (a) the transect averages and (b) the ΔCO (background-corrected CO) percentile ranges for each set of transects (Figure A.6). The error bars indicate the 95% confidence interval for the D_p slope. 1000 best fit lines from a Monte Carlo technique are shown in light gray. The average and slope and intercept with their respective 95% confidence interval for the Monte Carlo fits are shown in Table 3.1. The darker gray lines are the results of linear regressions with one sample removed. The solid black line is the linear regression for the points at the center of the error bars; the equation for this line is shown on each panel.

Table 3.1: Shown here are statistics on the various fits done in Figures 2 through 4. For rows where the left column is a rate of change ($\frac{d}{dt}$), the slope and intercept columns are an average from the Monte Carlo method of fitting based on the uncertainty of previously done linear regression.

Fit	Slope	95% Confidence	Intercept	Intercept Confidence
Transect Average $\frac{dD_p}{dt}$ [nm hr ⁻¹] vs. log(ΔOA_i) [log($\mu\text{g m}^{-3}$)]	4.3	1.1 to 7.9	-1.1	-9.9 to 7.5
ΔCO Percentile $\frac{dD_p}{dt}$ [nm hr ⁻¹] vs. log(ΔOA_i) [log($\mu\text{g m}^{-3}$)]	3.9	2.2 to 5.5	0.6	-3.4 to 4.6
Transect Average $\frac{d(\Delta N/\Delta CO)}{dt}$ [cm ⁻³ ppbv ⁻¹ hr ⁻¹ log($\mu\text{g m}^{-3}$) ⁻¹] vs. log(ΔOA_i) [log($\mu\text{g m}^{-3}$)]	-3.0	-17 to 11	-1.6	-45 to 42
ΔCO Percentile $\frac{d(\Delta N/\Delta CO)}{dt}$ [cm ⁻³ ppbv ⁻¹ hr ⁻¹ log($\mu\text{g m}^{-3}$) ⁻¹] vs. log(ΔOA_i) [log($\mu\text{g m}^{-3}$)]	-6.2	-11 to -1.9	9.6	-4.8 to 24
Transect Average OAER _i [$\mu\text{g m}^{-3}$ ppbv ⁻¹] vs. log(ΔOA_i) [log($\mu\text{g m}^{-3}$)]	0.17	0.10 to 0.25	-0.06	-0.26 to 0.14
ΔCO Percentile OAER _i [$\mu\text{g m}^{-3}$ ppbv ⁻¹] vs. log(ΔOA_i) [log($\mu\text{g m}^{-3}$)]	0.12	0.08 to 0.17	0.09	-0.02 to 0.22
Transect Average $\frac{d(OAER)}{dt}$ [$\mu\text{g m}^{-3}$ ppbv ⁻¹ hr ⁻¹] vs. log(ΔOA_i) [log($\mu\text{g m}^{-3}$)]	-0.03	-0.06 to -0.01	0.08	0.03 to 0.13
ΔCO Percentile $\frac{d(OAER)}{dt}$ [$\mu\text{g m}^{-3}$ ppbv ⁻¹ hr ⁻¹] vs. log(ΔOA_i) [log($\mu\text{g m}^{-3}$)]	-0.02	-0.04 to -0.01	0.04	0.01 to 0.08
Transect Average $\Delta O:\Delta C_i$ vs. log(ΔOA_i) [log($\mu\text{g m}^{-3}$)]	-0.07	-0.11 to -0.02	0.59	0.48 to 0.71
ΔCO Percentile $\Delta O:\Delta C_i$ vs. log(ΔOA_i) [log($\mu\text{g m}^{-3}$)]	-0.06	-0.07 to -0.04	0.57	0.54 to 0.61
Transect Average $\frac{d(\Delta O:\Delta C)}{dt}$ [hr ⁻¹] vs. log(ΔOA_i) [log($\mu\text{g m}^{-3}$)]	-0.01	-0.02 to 0.01	0.07	0.03 to 0.1
ΔCO Percentile $\frac{d(\Delta O:\Delta C)}{dt}$ [hr ⁻¹] vs. log(ΔOA_i) [log($\mu\text{g m}^{-3}$)]	-0.00	-0.01 to 0.01	0.05	0.02 to 0.08

The aerosol number enhancement ratio is moderately correlated with smoke age with an average Spearman correlation coefficient of -0.66 (Figure A.7); while D_p with smoke age had a very strong relationship with an average Spearman correlation coefficient of 0.81. The BBOP campaign also showed the number enhancement ratio to have less of a relationship with smoke age than diameter (Hodshire et al., 2021). If the diameter changes were primarily due to coagulation, we would expect that the more concentrated plumes would have a faster decrease in the number enhancement ratio (Sakamoto et al., 2016). The Pearson correlation coefficients between the rate of change of number enhancement ratio and ΔOA_i are -0.44 in the transect averages and -0.55 in the ΔCO percentiles. Thus, this quantifier gives a moderate relationship for both the rate of change of number enhancement ratio and D_p , which agrees with the results from Sakamoto et al. (2016) for plumes experiencing size distribution changes primarily through coagulation. Although the correlation coefficient for the transect averages gives a moderate relationship between the number enhancement ratio rate of change and ΔOA_i in the transect averages; taking into account the uncertainty of the rates of change in number enhancement ratio gives a non-statistically significant relationship with ΔOA_i of $-3.0 \text{ cm}^{-3} \text{ ppbv}^{-1} \text{ hr}^{-1} \log(\mu\text{g m}^{-3})^{-1}$ (Figure A.8a, Table 3.1). The large 95% confidence interval in the transect averages is in part due to the high uncertainty of rate of change of number enhancement ratio in the Williams Flats 8/6 sampling because of variability in number enhancement ratio from transect to transect (Figure A.7). In the ΔCO percentiles, there is a statistically significant relationship between the rate of number enhancement ratio change with smoke age and ΔOA_i with an average trend of $-6.2 \text{ cm}^{-3} \text{ ppbv}^{-1} \text{ hr}^{-1} \log(\mu\text{g m}^{-3})^{-1}$, although this may be influenced by mixing between percentiles (Figure A.8b, Table 3.1). In addition to the uncertainties in the linear regressions

discussed above, the number enhancement ratio trends may also be impacted by non-linearities, and changes in emissions.

The initial OAER increases as the initial Δ OA increases (Figure 3.2a,b). For the average values at the initial transect, this relationship has a slope of $0.17 \mu\text{g m}^{-3}\text{ppbv}^{-1} \log(\mu\text{g m}^{-3})^{-1}$ with a p-value less than 0.01 and a R of 0.91. When divided by Δ CO percentiles, the initial OAER increases with increasing initial Δ OA at a rate of $0.12 \mu\text{g m}^{-3}\text{ppbv}^{-1} (\mu\text{g m}^{-3})^{-1}$ with a p-value less than 0.01 and an R of 0.71. The lower OAER in dilute plumes suggests that there may be significant evaporation prior to the first transect (30 minutes to an hour downwind) in that is stronger in more dilute plumes, consistent with WE-CAN observations and simulations done in Akherati et al. (2022), and simulations of smoke plumes in Bian et al. (2017) and Hodshire et al. (2019). We cannot rule out that this strong to very strong initial OAER trend with initial OA is also impacted by the burn conditions, although this would require the fires with the most initially dilute plumes to have the lowest OA:CO emissions ratios. On the other hand, there is evidence that a significant fraction of smoke primary OA is semivolatile, such that we would expect evaporation of a fraction of this primary OA with dilution (May et al., 2013, 2015).

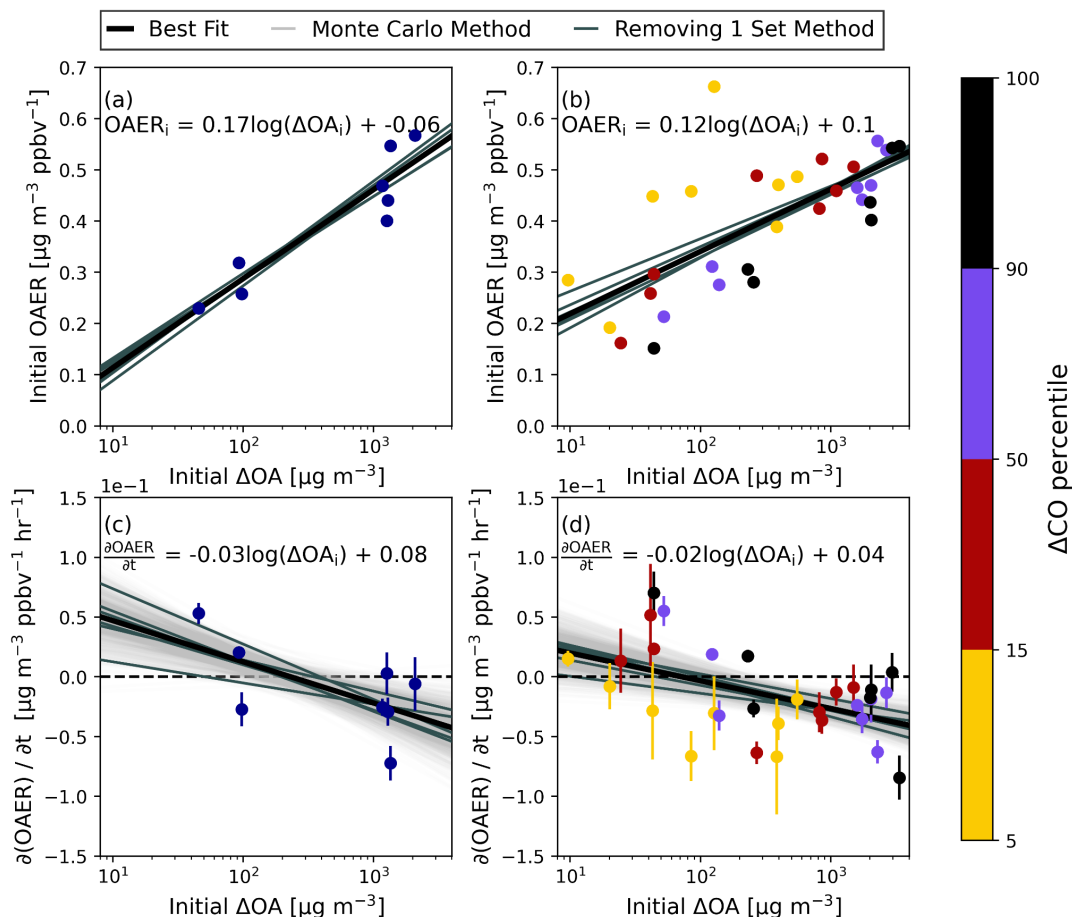


Figure 3.2: Initial initial OAER versus initial ΔOA for (a) the transect averages and (b) by ΔCO percentile with an OLS regression line in gray. The statistics for this fit are shown in Table 3.1. The OAER trends with smoke age based on OLS fitting as a function of ΔOA_i for (c) the transect averages and (d) by ΔCO percentile respectively. On each panel, the best fit line for the points is shown in solid black with the equation of this line shown on the panel. The darker gray lines are the results of linear regressions with one sample removed. On (c) and (d), 1000 best fit lines from a Monte Carlo technique are also included in light gray with statistics for these fits shown in Table 3.1. The black dashed line on (c) and (d) is the $y=0$ line.

With aging, OAER either increases, decreases or remains about the same, with a moderate to strong negative correlation with increasing initial ΔOA (Pearson R of -0.62 and -0.51 in the transect averages and ΔCO percentiles). The average Monte Carlo slope is $-0.03 \mu\text{g m}^{-3}\text{ppbv}^{-1} \text{hr}^{-1} \log(\mu\text{g m}^{-3})^{-1}$ in the transect averages and $-0.02 \mu\text{g m}^{-3}\text{ppbv}^{-1} \text{hr}^{-1} \log(\mu\text{g m}^{-3})^{-1}$ in ΔCO percentiles (Figure 3.2c,d); the 95% confidence intervals are in Table 3.1 and do not cross zero. The positive slopes seen at lower concentrations combined with the first transect being at

least 30 minutes downwind is supported by prior theoretical work (Figure A.9). This prior work showed that for dilute plumes, there was an initial decrease in OAER followed by an increase in OAER starting after about 30 minutes (Bian et al., 2017; Hodshire et al., 2019b). Both the WE-CAN and BBOP campaign showed no significant change in OAER as the plumes aged (Hodshire et al., 2021; Palm et al., 2020). Two samplings included here, Shady 7/25 and Williams Flats 8/7 P2, have no statistically significant change in OAER as the smoke ages; OAER is variable between transects for Shady 7/25, however for Williams Flats 8/7 P2 OAER is consistent as the smoke ages (Figure A.9). Palm et al. (2020) showed that dilution driven evaporation of POA was a source of SOA in the fires, creating an overall balance in the OAER as the smoke aged, this may be what is occurring in the Williams Flats 8/7 P2 sampling. The reduction of OAER seen at high concentrations was not observed in WE-CAN (Palm et al., 2020), however the upper end of concentrations shown here for FIREX-AQ are greater than those from WE-CAN. Although there is likely SOA formation occurring in the concentrated plumes, it is not enough to increase the OAER relative to the initial values suggesting that the dilution driven evaporation of semi-volatile species is the dominant process in the concentrated FIREX-AQ smoke plumes (Hodshire et al., 2019a). The decrease may also be due to a lack of chemical aging occurring in these plumes (May et al., 2013); however, we do not have enough evidence to say for certain that slow photochemistry is the reason for the decrease in OAER. Despite the decrease in OAER for concentrated fires, which would act to decrease the particle diameter, the concentrated fires still see more growth (Figure 3.1), which highlights the role of coagulation for growth and will be investigated further later.

The initial values of $\Delta O:\Delta C$ increase as plume concentration decreases with a very strong relationship (Figure 3.3a-b). In the transect averages, this trend is $-0.07 \log(\mu\text{g m}^{-3})^{-1}$ (p-value <

0.01, $R = 0.84$) and in the ΔCO percentiles this trend is also $-0.06 \log(\mu\text{g m}^{-3})^{-1}$ ($p\text{-value} < 0.01$, $R = 0.84$). $\Delta\text{O}:\Delta\text{C}$ is higher in SOA than the evaporating POA (DeCarlo et al., 2008; Hodshire et al., 2019a, 2021). Additionally, the evaporating POA has been found to have lower $\Delta\text{O}:\Delta\text{C}$ than the remaining POA that does not evaporate (Akherati et al., 2022). This suggests that in dilute plumes there may be faster evaporation and/or SOA formation prior to the first transect. Higher initial $\Delta\text{O}:\Delta\text{C}$ in dilute plumes complements them tending to have lower initial OAER (Figure 3.2a-b); both indicate faster evaporation prior to the first transect in dilute plumes. There was evidence for this in the WE-CAN plumes as well (Akherati et al., 2022). In simulations of the WE-CAN plumes, Akherati et al. (2022) showed that it is likely that the POA evaporating prior to the first transect has a lower $\Delta\text{O}:\Delta\text{C}$, leaving the remaining POA with higher $\Delta\text{O}:\Delta\text{C}$. Further, the more-dilute plumes contained a higher fraction of SOA at the first transect, further increasing the $\Delta\text{O}:\Delta\text{C}$ of the more-dilute plumes. Our results appear to be consistent with these findings of Akherati et al. (2022).

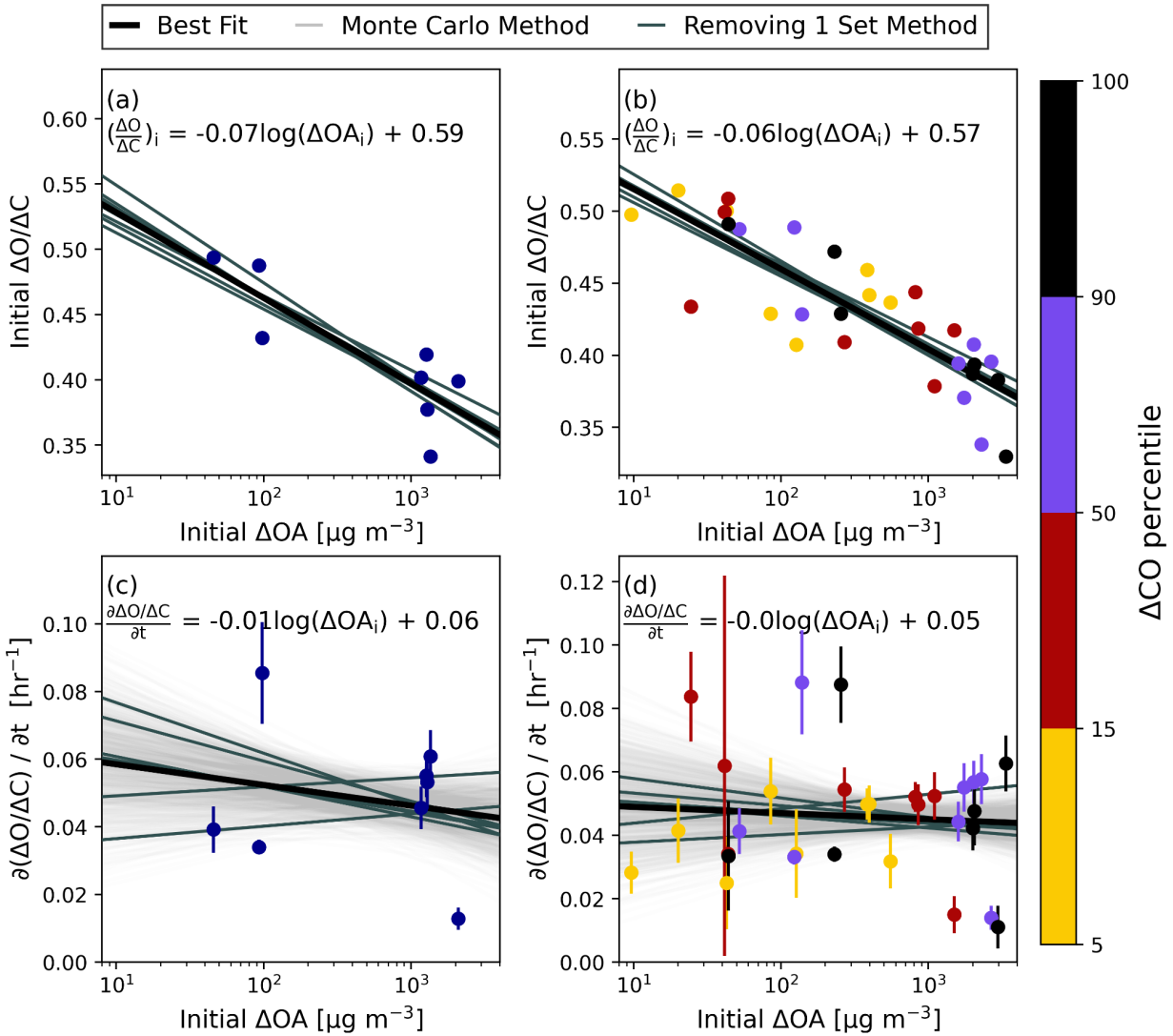


Figure 3.3: The initial $\Delta O:\Delta C$ at the first transect versus initial ΔOA for (a) the transect averages and (b) by ΔCO percentile. The linear fit slopes of $\Delta O:\Delta C$ with smoke age versus ΔOA_i for (c) the transect averages and (d) by ΔCO percentile. On each panel, the best fit line for the points is shown in solid black with the equation of this line shown on the panel. The darker gray lines are the results of linear regressions with one sample removed. On (c) and (d), 1000 best fit lines from a Monte Carlo technique are also included in light gray with statistics for these fits shown in Table 3.1.

All plumes and ΔCO percentiles within plumes show a very strong increase in $\Delta O:\Delta C$ with smoke age with Spearman correlation coefficients of 0.93 in the transect averages and 0.96 in the ΔCO percentiles (Figure A.10), but there is no significant trend for the rate at which $\Delta O:\Delta C$ increases as the plume ages with the initial plume concentration (ΔOA_i) in either case

(Figure 3.3c-d, Table 3.1). Therefore, the less concentrated plumes and portions of plumes tend to continue to have higher $\Delta O:\Delta C$ ratios as the plume ages. Since the dilute plumes had a higher initial $\Delta O:\Delta C$, they continue to have higher $\Delta O:\Delta C$ values than the more-concentrated plumes at each plume age. The BBOP campaign had a moderate relationship of $\Delta O:\Delta C$ with smoke age (Hodshire et al., 2021). From the comprehensive review paper, Hodshire et al. (2019a), it shows that most field campaigns nearly always observe $\Delta O:\Delta C$ increasing with smoke age. Akherati et al. (2022) ran simulations for the WE-CAN campaign, which also observed increases in $\Delta O:\Delta C$ with smoke age. They found that dilution driven evaporation of semi-volatile POA played the strongest role of increasing $\Delta O:\Delta C$ (as opposed to SOA formation) (Akherati et al., 2022). It is possible that this dilution-driven evaporation is what is dominating the $\Delta O:\Delta C$ increases and OAER decreases seen in the concentrated FIREX-AQ smoke plumes. In the cases where there is an increase or no change in OAER and an increase in $\Delta O:\Delta C$ with smoke age, there is likely both dilution driven POA evaporation and significant SOA formation from semi-volatile organic compounds and volatile organic compounds.

3.2 Estimating the Drivers of Observed Growth

Coagulation is the primary cause of growth in these smoke plumes with the rate being impacted by dilution, as shown by the solid line in Figure 3.4. With the exception of July 29, coagulation explains the majority of the growth seen in the smoke plumes. For the days where coagulation did explain the majority of the growth, the modeled coagulation often represented the growth of the median diameter within the uncertainty of the observed median diameter (Figure 3.4). After the first transect (where the model and observation are forced to be equal), the modeled and observed median diameters have a very strong relationship with an average Pearson correlation coefficient of 0.82. Overall across all cases, the mean absolute error after the first

transect is 7 nm; however, this error is within the uncertainty range of the measurements. Additionally, coagulation alone does well at estimating the rate of change of the median diameter with smoke age, with a very strong Pearson correlation coefficient between the modeled dD_p/dt and the observed dD_p/dt of 0.8 (Figure A.11). Our findings are supportive of estimations from Hodshire et al. (2021) and Sakamoto et al. (2016) that coagulation is the dominant process in changing the diameter in smoke plumes. The dilution rate also impacts the rates of the simulated D_p growth. Williams Flats 8/7 P2 is the slowest diluting plume with a dilution rate of 0.09 hr^{-1} with an average simulated growth rate of 22 nm hr^{-1} ; however, the Williams Flats 8/7 P1 simulation, which had a similar initial number concentration and modal width, diluted quicker at 0.43 hr^{-1} only had an average simulated growth rate of 15 nm hr^{-1} due to a decreased growth rate after the first two hours. In both cases, the simulation accurately represents the observed growth rates of 20 nm hr^{-1} in Williams Flats 8/7 P2 and 14 nm hr^{-1} in P1, supportive of findings in Sakamoto et al. (2016) that a plume with a faster dilution rate may have a slower coagulation rate due to the decrease in number concentration from dilution.

The agreement between modeled and observed D_p is potentially impacted by some of the assumptions that we made during our analysis, including assuming a linear function for the LAS saturation correction extension (Figure A.2) and assuming a non-size-dependent evaporation correction (Figure A.3). If we were to assume no LAS saturation correction was needed, the observed median diameter growth is underpredicted by the model (lower initial particle concentrations, so slower coagulation), whereas if we assume a quadratic function for the LAS saturation correction extension, the observed median diameter is overpredicted by the model (higher initial particle concentrations, so faster coagulation) (Figure A.12). Changing from the non-size-dependent evaporation correction to a size-dependent evaporation correction based on

Figure A.3b, does not change the agreement of the modeled and observed median diameters (Figure A.13).

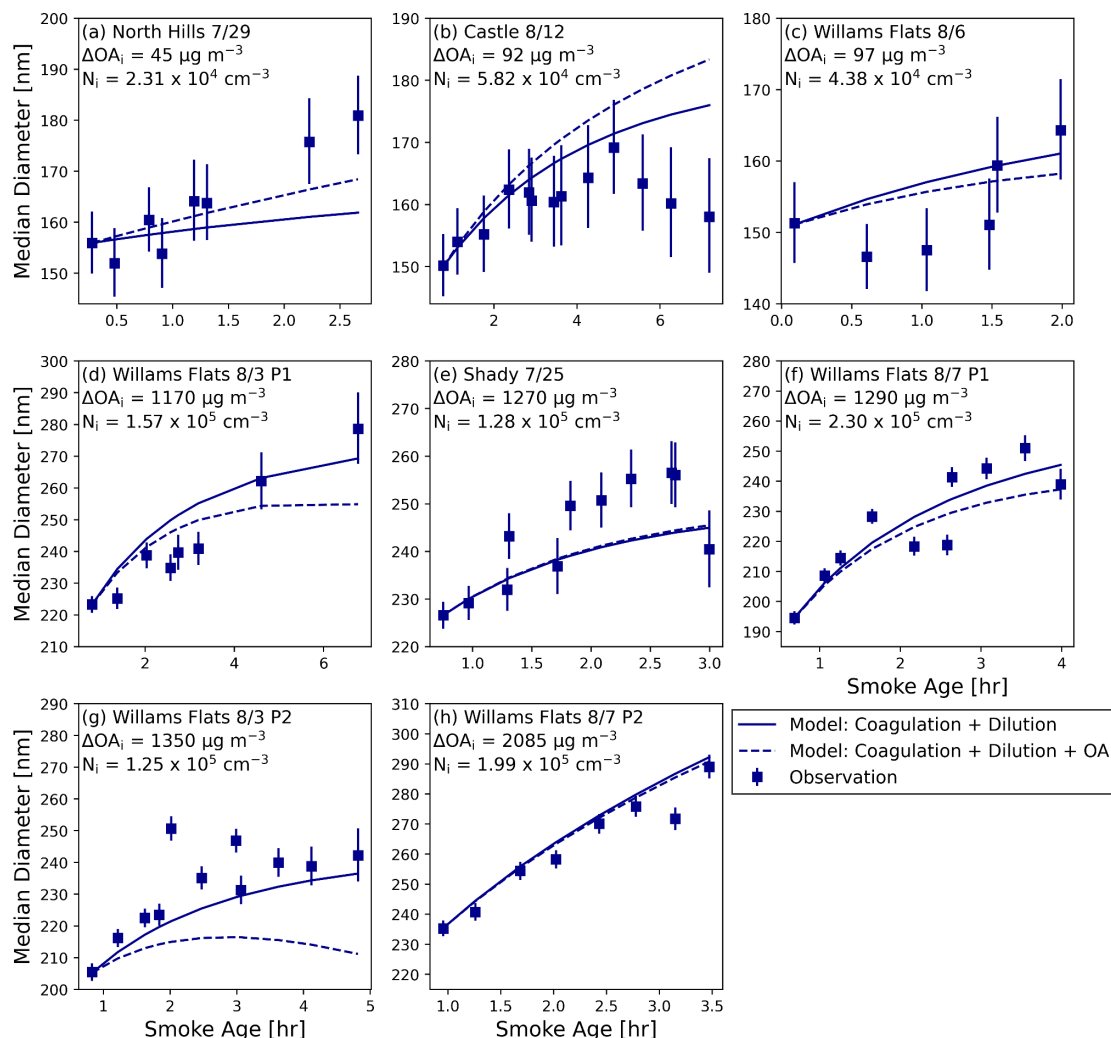


Figure 3.4: The observed median diameter (D_p) (points), modeled D_p due to coagulation and dilution alone (solid line), and modeled D_p due to coagulation and dilution plus diameter changes due to OA evaporation/condensation (dashed line) as a function of smoke age for each of the eight smoke plumes used in our analysis. The error bars represent the standard deviation of D_p within the transect. On each panel is ΔOA_i , and the aerosol number concentration of particles between 50 nm and 800 nm measured at the first transect (N_i). (a)-(h) are in order of increasing ΔOA_i .

The observed trends in the number enhancement ratio are noisier than the trends in D_p , but the model still is able to capture some of the reduction in number as a result of coagulation (Figure A.14). The average Spearman and Pearson correlation coefficients between modeled and

observed number enhancement ratio are 0.54 and 0.51, respectively, a moderate relationship. These correlation values are negatively impacted by poor correlations between the model and observations on North Hills 7/29 and Williams Flats 8/6. The model did have a decrease in number enhancement ratio on both of these days; however, the noise in the observations resulted in slightly negative correlation between the modeled and observed number enhancement ratio. The removal of these two samplings increases the average Pearson correlation coefficient to 0.81, a very strong relationship, similar to that between the modeled and observed D_p . This result suggests the model is reasonably simulating the decrease in number enhancement ratio due to coagulation, but it is unclear why the observed trend in the number enhancement ratio is more noisy than the observed trend in median diameter.

In some cases, OA condensation/evaporation can further explain some of the growth; however, this effect is often an adjustment that is smaller in magnitude than the variability of the measurements. OA condensation/evaporation was included in the model based on the observed trends in OA (Figure 3.2c) and Eq. 2.5. Consistent with the OAER trends, net condensation grows the particles in comparison to the coagulation-only model diameter in 3 cases, and net evaporation shrinks the model particle diameter in 5 cases. The North Hills 7/29 case had the largest improvement as a result of including the observed condensation/evaporation effects. On this day, coagulation only increased the diameter by 5 nm, while coagulation and condensation combined increased the diameter by 15 nm, which was closer to the observed growth of 25 nm. Overall, the changes due to including the OA condensation/evaporation were often small, and this is reflected in the mean absolute error only changing from 11 nm to 9 nm (Figure 3.4). This relatively small change in model performance suggests that the condensation/evaporation had a minor effect on the changing of the diameter in these plumes; however, due to uncertainties in

the diameter measurements, it is unclear if including condensation/evaporation significantly improves the model. We recognize that there is uncertainty in the role of condensation/evaporation due to the imperfect Lagrangian sampling of the plumes as well as uncertainties in the linear regressions of OAER vs. age. However, since some plumes were sampled more than once on the same day, and the times of day also varied, we think condensation/evaporation has a minor effect due to it not explaining a majority of the growth in any of the eight simulations. In some prior works, POA evaporation roughly balanced SOA formation, leading to no net change in OAER. In these cases condensation/evaporation would have no effect on the median diameter and coagulation would be the primary cause of growth (Bian et al., 2017; Hodshire et al., 2019b, a; May et al., 2015; Palm et al., 2020). Here we have shown that even in cases where OAER is changing as the plume ages, coagulation is still the primary mechanism through which the diameter changes and diameter changes due to condensation/evaporation are minor.

The modeled results when segregated by ΔCO percentile generally show an overprediction of growth in the highest percentile bins (both with coagulation only and also when condensation/evaporation are added), and an underprediction of growth in the lowest percentile bin (Figure 3.5). On average, the mean bias for the simulation without OA condensation/evaporation is larger than the typical variability of the median diameter measurements at -15 nm and 13 nm in the 5-15 and 90-100 ΔCO percentiles, respectively. The Pearson correlation coefficients between the modeled and observed dD_p/dt are weak (0.29) in the 5-15 ΔCO percentile and very strong (0.83) in the 90-100 ΔCO percentile (albeit with an model overprediction of growth). While the 90-100 ΔCO percentile has a similar correlation between modeled and observed dD_p/dt as the transect averages, the correlation in the 5-15 ΔCO percentile

is weaker due to less coherent growth trends in the observations and influence from the other percentile bins. Similar to the transect averaged results, including OA condensation/evaporation based on the observed changes in OAER only changes the model agreement within the uncertainty of the measurements with a mean bias of 11 nm in the 90-100 ΔCO percentile and -18 nm in the 5-15 ΔCO percentile.

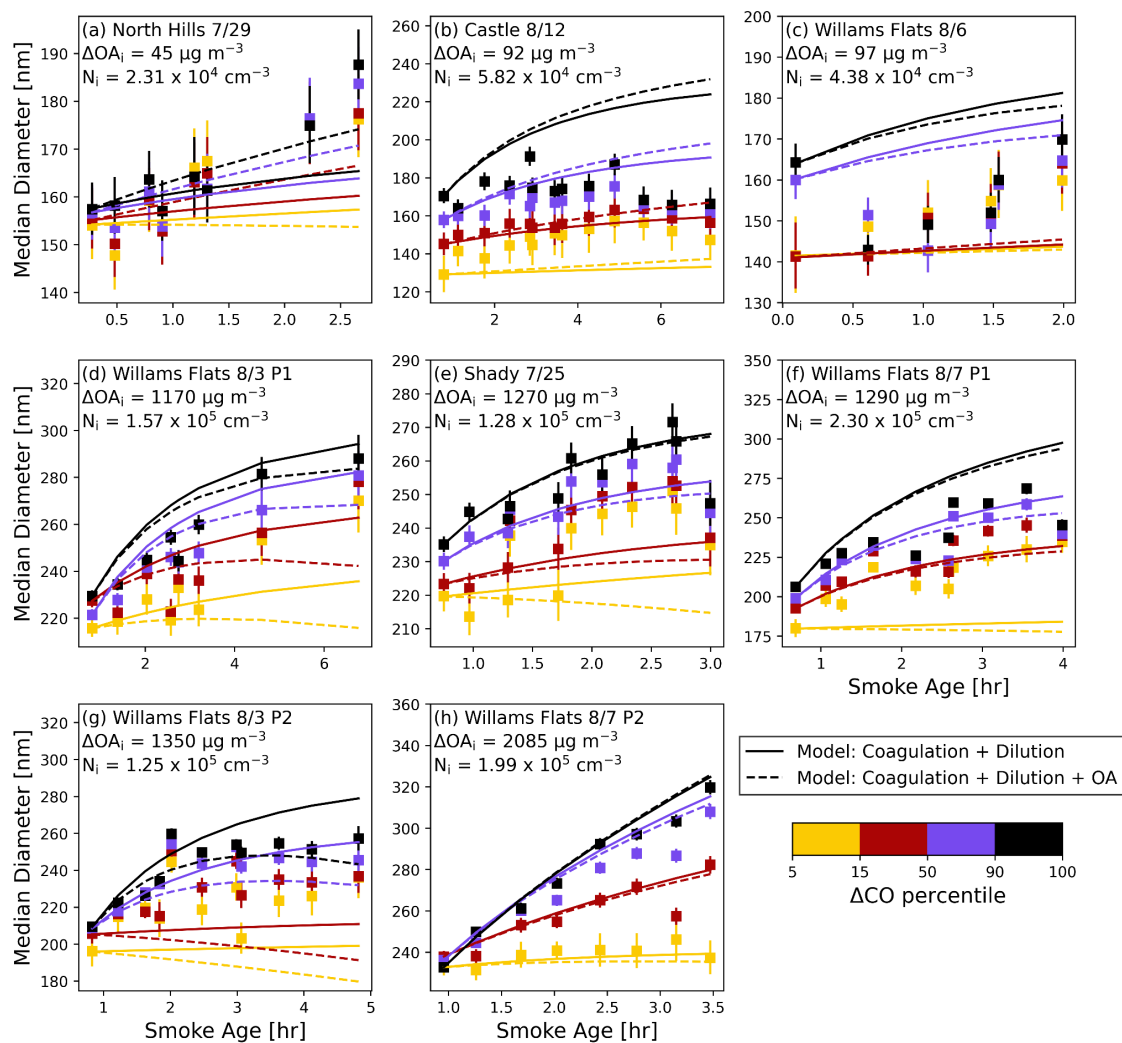


Figure 3.5: The observed (points), coagulation modeled (solid line), and coagulation plus changes due to OA evaporation/condensation (dashed line) median diameter as a function of smoke age for each of the eight smoke plumes used in our analysis colored by ΔCO percentile. The error bars represent the standard deviation of D_p within the transect. Shown inset is the ΔOA measured at the first transect (ΔOA_i) in $\mu g m^{-3}$, and the aerosol number concentration of particles greater than 100 nm measured at the first transect (N_i) in $\# cm^{-3}$. (a)-(h) are in order of increasing initial ΔOA .

The larger magnitude of bias in the extremities of the ΔCO percentiles than that seen in the transect averages suggests that mixing between percentile regions of the plumes is occurring on a time scale slow enough that there are apparent differences between the dilute and concentrated portions of the smoke plume, but the mixing is happening too quickly for the core and edge of the plume to be treated separately when looking at several hours of aging. Mixing times between the core and edge of the plume were calculated based on wind standard deviation derived stability class and Gaussian plume relations. The majority of mixing times tend to be around 2 to 5 hours as shown in Table 3.2. We believe that these times are supportive of the results in Figure 3.5, since it is comparable to the length of time the plane may have been sampling a plume. The exception to this is the mixing times for August 7, which are longer than in the other cases (particularly for 8/7 P2). The mixing times on this day are longer due to less variability in the winds resulting in a more stable stability class. Williams Flats 8/7 P2, which had the longest mixing time at 25 hr, was the only case where D_p in both the 5-15 and 90-100 ΔCO percentiles was simulated within the uncertainty of the measurements, which is additional evidence that in this case the mixing was slow enough that treating the percentiles as separate was a valid assumption. Williams Flats 8/7 P1 also had a longer mixing time at about 9 hr; however, there was large overprediction in the 90-100 ΔCO percentile (26 nm) and large underestimation in the 5-15 ΔCO percentile (-33 nm). There could be greater vertical mixing in the plume on this day not captured by the horizontal mixing time. Vertical mixing not captured here may also influence results on other days as well; for example, vertical mixing in the plume on August 3 was evident in large eddy simulations (LES) of the first pass on this day (Wang et al., 2021). In the LES simulation, dilution and physical mixing strongly impacted the chemistry within the smoke plume, but this study did not examine how the mixing impacted the particle

diameters in the smoke plume (Wang et al., 2021). A case study outside of FIREX-AQ using LIDAR data reported that turbulent eddies had a larger influence on the backscatter variance and concentrations on the edges of a smoke plume than in the center of the plume (Lareau and Clements, 2017), which may be evident in our modeling results here where the 5-15 Δ CO percentile modeled diameter generally has more disparity from the observations than the 90-100 Δ CO percentile.

Table 3.2: The distance between the average location of the 90-100 Δ CO percentile (Core) and the innermost location in the 5 to 15 percentile bin (Edge) and the corresponding time it takes for the plume to mix that distance.

Flight	Core Edge Distance [m]	Mixing Time [hr]
7/25	6291	3.8
7/29	2695	1.4
8/3 1	6321	4.0
8/3 2	11470	4.6
8/6	8604	3.1
8/7 1	10841	8.9
8/7 2	13153	25.1
8/12	12786	2.4

Chapter 4

Conclusions

Using data from eight pseudo-Lagrangian samplings from western US wildfires during the FIREX-AQ campaign and simulations of growth using a sectional aerosol microphysics model, we examined the impact of OA mass concentration on observed aerosol size distribution, organic aerosol enhancement ratio (OAER), and $\Delta\text{O}:\Delta\text{C}$ evolution in the first 3 to 7 hr of physical smoke aging. Observations showed that despite plumes with greater concentrations tending to have more evaporation, they have more diameter growth. Our subsequent simulations of the smoke plumes indicate that the diameter growth is dominated by coagulation. Although coagulation explained the majority of the growth, the rate at which number enhancement ratio decreased was not significantly correlated to initial ΔOA (ΔOA_i). Increased understanding of how the emissions changed as the smoke was being sampled due to deviations from true Lagrangian sampling, and improved understanding of how the LAS saturates at high concentrations may help to resolve discrepancies between the observed trends in aerosol diameter and number enhancement ratio. At the first transect, initial OAER and initial $\Delta\text{O}:\Delta\text{C}$ suggest that less concentrated plumes have faster evaporation and SOA formation prior to the first transect. While $\Delta\text{O}:\Delta\text{C}$ always increased in the smoke plumes with no correlation to the plume concentration, rates in OAER change as the plume ages vary with plume concentration such that net evaporation as the plume ages is more likely in the more concentrated plumes. Dilution-driven evaporation is likely important in these OAER decreases and $\Delta\text{O}:\Delta\text{C}$ increases seen in these smoke plumes. While in plumes with no significant OAER change, there is likely a balance between POA evaporation and SOA formation. Additional modeling of OA and its

composition would improve understanding of the relative roles of evaporation and SOA formation in plumes of varying concentrations. While dividing the plume into dilute and concentrated sections based on ΔCO percentiles, showed changes in diameter, number enhancement ratio, and OAER with smoke age to be dependent on ΔOA_i , physical mixing within the plume limits the ability to simulate ΔCO percentiles independently especially on the edges of smoke plumes, which experienced more growth than simulated. Due to physical mixing, using location within the plume to extend the range of plume concentrations may limit the ability to apply our percentile based results to plumes with that average concentration. Lagrangian sampling of a wider range of plumes, or sampling plumes under very stable conditions with limited mixing, would help to improve the understanding of how smoke plume concentration influences its evolution.

Future work includes using a dispersion-resolving model with online chemistry and aerosol microphysics schemes to better examine the results found here relating to in-plume gradients and OA evaporation/condensation. Simulations of this type would also help to better quantify vertical and horizontal mixing occurring in the smoke plumes. Additionally, continued work in understanding how the details of varying species emission ratios impact the plume aging would be beneficial as our results here do not take into consideration fuel types.

References

- Akagi, S. K., Yokelson, R. J., Wiedinmyer, C., Alvarado, M. J., Reid, J. S., Karl, T., Crounse, J. D., and Wennberg, P. O.: Emission factors for open and domestic biomass burning for use in atmospheric models, *Atmospheric Chem. Phys.*, 11, 4039–4072, <https://doi.org/10.5194/acp-11-4039-2011>, 2011.
- Akagi, S. K., Craven, J. S., Taylor, J. W., McMeeking, G. R., Yokelson, R. J., Burling, I. R., Urbanski, S. P., Wold, C. E., Seinfeld, J. H., Coe, H., Alvarado, M. J., and Weise, D. R.: Evolution of trace gases and particles emitted by a chaparral fire in California, *Atmospheric Chem. Phys.*, 12, 1397–1421, <https://doi.org/10.5194/acp-12-1397-2012>, 2012.
- Akherati, A., He, Y., Garofalo, L. A., Hodshire, A. L., Farmer, D. K., Kreidenweis, S. M., Permar, W., Hu, L., Fischer, E. V., Jen, C. N., Goldstein, A. H., Levin, E. J. T., DeMott, P. J., Campos, T. L., Flocke, F., Reeves, J. M., Toohey, D. W., Pierce, J. R., Jathar, S. H.: Dilution and Photooxidation Driven Processes Explain the Evolution of Organic Aerosol in Wildfire Plumes, submitted to *Environmental Science: Atmospheres*, 2021.
- Albrecht, B. A.: Aerosols, Cloud Microphysics, and Fractional Cloudiness, *Science*, <https://doi.org/10.1126/science.245.4923.1227>, 1989.
- Alonso-Blanco, E., Calvo, A. I., Pont, V., Mallet, M., Fraile, R., and Castro, A.: Impact of Biomass Burning on Aerosol Size Distribution, Aerosol Optical Properties and Associated Radiative Forcing, *Aerosol Air Qual. Res.*, 14, 708–724, <https://doi.org/10.4209/aaqr.2013.05.0163>, 2014.
- Arya, S. P.: *Air Pollution Meteorology and Dispersion*, Oxford University Press, 1999.
- Bian, Q., Jathar, S. H., Kodros, J. K., Barsanti, K. C., Hatch, L. E., May, A. A., Kreidenweis, S. M., and Pierce, J. R.: Secondary organic aerosol formation in biomass-burning plumes: theoretical analysis of lab studies and ambient plumes, *Atmospheric Chem. Phys.*, 17, 5459–5475, <https://doi.org/10.5194/acp-17-5459-2017>, 2017.
- Bond, T. C., Doherty, S. J., Fahey, D. W., Forster, P. M., Berntsen, T., DeAngelo, B. J., Flanner, M. G., Ghan, S., Kärcher, B., Koch, D., Kinne, S., Kondo, Y., Quinn, P. K., Sarofim, M. C., Schultz, M. G., Schulz, M., Venkataraman, C., Zhang, H., Zhang, S., Bellouin, N., Guttikunda, S. K., Hopke, P. K., Jacobson, M. Z., Kaiser, J. W., Klimont, Z., Lohmann, U., Schwarz, J. P., Shindell, D., Storelvmo, T., Warren, S. G., and Zender, C. S.: Bounding the role of black carbon in the climate system: A scientific assessment, *J. Geophys. Res. Atmospheres*, 118, 5380–5552, <https://doi.org/10.1002/jgrd.50171>, 2013.
- Capes, G., Johnson, B., McFiggans, G., Williams, P. I., Haywood, J., and Coe, H.: Aging of biomass burning aerosols over West Africa: Aircraft measurements of chemical composition, microphysical properties, and emission ratios, *J. Geophys. Res. Atmospheres*, 113, <https://doi.org/10.1029/2008JD009845>, 2008.
- Carrico, C. M., Petters, M. D., Kreidenweis, S. M., Collett Jr., J. L., Engling, G., and Malm, W. C.: Aerosol hygroscopicity and cloud droplet activation of extracts of filters from biomass

burning experiments, *J. Geophys. Res. Atmospheres*, 113, <https://doi.org/10.1029/2007JD009274>, 2008.

Charlson, R. J., Langner, J., Rodhe, H., Leovy, C. B., and Warren, S. G.: Perturbation of the northern hemisphere radiative balance by backscattering from anthropogenic sulfate aerosols, *Tellus Dyn. Meteorol. Oceanogr.*, 43, 152–163, <https://doi.org/10.3402/tellusa.v43i4.11944>, 1991.

Cubison, M. J., Ortega, A. M., Hayes, P. L., Farmer, D. K., Day, D., Lechner, M. J., Brune, W. H., Apel, E., Diskin, G. S., Fisher, J. A., Fuelberg, H. E., Hecobian, A., Knapp, D. J., Mikoviny, T., Riemer, D., Sachse, G. W., Sessions, W., Weber, R. J., Weinheimer, A. J., Wisthaler, A., and Jimenez, J. L.: Effects of aging on organic aerosol from open biomass burning smoke in aircraft and laboratory studies, *Atmospheric Chem. Phys.*, 11, 12049–12064, <https://doi.org/10.5194/acp-11-12049-2011>, 2011.

DeCarlo, P. F., Dunlea, E. J., Kimmel, J. R., Aiken, A. C., Sueper, D., Crouse, J., Wennberg, P. O., Emmons, L., Shinozuka, Y., Clarke, A., Zhou, J., Tomlinson, J., Collins, D. R., Knapp, D., Weinheimer, A. J., Montzka, D. D., Campos, T., and Jimenez, J. L.: Fast airborne aerosol size and chemistry measurements above Mexico City and Central Mexico during the MILAGRO campaign, *Atmospheric Chem. Phys.*, 8, 4027–4048, <https://doi.org/10.5194/acp-8-4027-2008>, 2008.

Decker, Z. C. J., Wang, S., Bourgeois, I., Campuzano Jost, P., Coggon, M. M., DiGangi, J. P., Diskin, G. S., Flocke, F. M., Franchin, A., Fredrickson, C. D., Gkatzelis, G. I., Hall, S. R., Halliday, H., Hayden, K., Holmes, C. D., Huey, L. G., Jimenez, J. L., Lee, Y. R., Lindaas, J., Middlebrook, A. M., Montzka, D. D., Neuman, J. A., Nowak, J. B., Pagonis, D., Palm, B. B., Peischl, J., Piel, F., Rickly, P. S., Robinson, M. A., Rollins, A. W., Ryerson, T. B., Sekimoto, K., Thornton, J. A., Tyndall, G. S., Ullmann, K., Veres, P. R., Warneke, C., Washenfelder, R. A., Weinheimer, A. J., Wisthaler, A., Womack, C., and Brown, S. S.: Novel Analysis to Quantify Plume Crosswind Heterogeneity Applied to Biomass Burning Smoke, *Environ. Sci. Technol.*, 55, 15646–15657, <https://doi.org/10.1021/acs.est.1c03803>, 2021.

Evans, J. D.: *Straightforward Statistics for the Behavioral Sciences*, Brooks/Cole Publishing Company, 632 pp., 1996.

Ford, B., Val Martin, M., Zelasky, S. E., Fischer, E. V., Anenberg, S. C., Heald, C. L., and Pierce, J. R.: Future Fire Impacts on Smoke Concentrations, Visibility, and Health in the Contiguous United States, *GeoHealth*, 2, 229–247, <https://doi.org/10.1029/2018GH000144>, 2018.

Fuchs, N. A.: *The Mechanics of Aerosols*, Rev. and enl. ed., Pergamon Press, Oxford, xiii, 408 pp., 1964.

Gan, R. W., Ford, B., Lassman, W., Pfister, G., Vaidyanathan, A., Fischer, E., Volckens, J., Pierce, J. R., and Magzamen, S.: Comparison of wildfire smoke estimation methods and associations with cardiopulmonary-related hospital admissions, *GeoHealth*, 1, 122–136, <https://doi.org/10.1002/2017GH000073>, 2017.

Gilman, J. B., Lerner, B. M., Kuster, W. C., Goldan, P. D., Warneke, C., Veres, P. R., Roberts, J. M., de Gouw, J. A., Burling, I. R., and Yokelson, R. J.: Biomass burning emissions and potential air quality impacts of volatile organic compounds and other trace gases from fuels common in the US, *Atmospheric Chem. Phys.*, 15, 13915–13938, <https://doi.org/10.5194/acp-15-13915-2015>, 2015.

Hatch, L. E., Luo, W., Pankow, J. F., Yokelson, R. J., Stockwell, C. E., and Barsanti, K. C.: Identification and quantification of gaseous organic compounds emitted from biomass burning using two-dimensional gas chromatography–time-of-flight mass spectrometry, *Atmospheric Chem. Phys.*, 15, 1865–1899, <https://doi.org/10.5194/acp-15-1865-2015>, 2015.

Haywood, J. and Boucher, O.: Estimates of the direct and indirect radiative forcing due to tropospheric aerosols: A review, *Rev. Geophys.*, 38, 513–543, <https://doi.org/10.1029/1999RG000078>, 2000.

Hecobian, A., Liu, Z., Hennigan, C. J., Huey, L. G., Jimenez, J. L., Cubison, M. J., Vay, S., Diskin, G. S., Sachse, G. W., Wisthaler, A., Mikoviny, T., Weinheimer, A. J., Liao, J., Knapp, D. J., Wennberg, P. O., Kürten, A., Crouse, J. D., Clair, J. S., Wang, Y., and Weber, R. J.: Comparison of chemical characteristics of 495 biomass burning plumes intercepted by the NASA DC-8 aircraft during the ARCTAS/CARB-2008 field campaign, *Atmospheric Chem. Phys.*, 11, 13325–13337, <https://doi.org/10.5194/acp-11-13325-2011>, 2011.

Hinds, W. C.: *Aerosol Technology: Properties, Behavior, and Measurement of Airborne Particles*, Wiley, 512 pp., 1999.

Hobbs, P. V., Sinha, P., Yokelson, R. J., Christian, T. J., Blake, D. R., Gao, S., Kirchstetter, T. W., Novakov, T., and Pilewskie, P.: Evolution of gases and particles from a savanna fire in South Africa, *J. Geophys. Res. Atmospheres*, 108, <https://doi.org/10.1029/2002JD002352>, 2003.

Hodshire, A. L., Akherati, A., Alvarado, M. J., Brown-Steiner, B., Jathar, S. H., Jimenez, J. L., Kreidenweis, S. M., Lonsdale, C. R., Onasch, T. B., Ortega, A. M., and Pierce, J. R.: Aging Effects on Biomass Burning Aerosol Mass and Composition: A Critical Review of Field and Laboratory Studies, *Environ. Sci. Technol.*, 53, 10007–10022, <https://doi.org/10.1021/acs.est.9b02588>, 2019a.

Hodshire, A. L., Bian, Q., Ramnarine, E., Lonsdale, C. R., Alvarado, M. J., Kreidenweis, S. M., Jathar, S. H., and Pierce, J. R.: More Than Emissions and Chemistry: Fire Size, Dilution, and Background Aerosol Also Greatly Influence Near-Field Biomass Burning Aerosol Aging, *J. Geophys. Res. Atmospheres*, 124, 5589–5611, <https://doi.org/10.1029/2018JD029674>, 2019b.

Hodshire, A. L., Ramnarine, E., Akherati, A., Alvarado, M. L., Farmer, D. K., Jathar, S. H., Kreidenweis, S. M., Lonsdale, C. R., Onasch, T. B., Springston, S. R., Wang, J., Wang, Y., Kleinman, L. I., Sedlacek III, A. J., and Pierce, J. R.: Dilution impacts on smoke aging: evidence in Biomass Burning Observation Project (BBOP) data, *Atmospheric Chem. Phys.*, 21, 6839–6855, <https://doi.org/10.5194/acp-21-6839-2021>, 2021.

Huffman, J. A., Docherty, K. S., Aiken, A. C., Cubison, M. J., Ulbrich, I. M., DeCarlo, P. F., Sueper, D., Jayne, J. T., Worsnop, D. R., Ziemann, P. J., and Jimenez, J. L.: Chemically-resolved aerosol volatility measurements from two megacity field studies, *Atmospheric Chem. Phys.*, 9, 7161–7182, <https://doi.org/10.5194/acp-9-7161-2009>, 2009.

Jacobson, M. Z.: Strong radiative heating due to the mixing state of black carbon in atmospheric aerosols, *Nature*, 409, 695–697, <https://doi.org/10.1038/35055518>, 2001.

Jalava, P. I., Salonen, R. O., Hälinen, A. I., Penttinen, P., Pennanen, A. S., Sillanpää, M., Sandell, E., Hillamo, R., and Hirvonen, M.-R.: In vitro inflammatory and cytotoxic effects of size-segregated particulate samples collected during long-range transport of wildfire smoke to Helsinki, *Toxicol. Appl. Pharmacol.*, 215, 341–353, <https://doi.org/10.1016/j.taap.2006.03.007>, 2006.

Janhäll, S., Andreae, M. O., and Pöschl, U.: Biomass burning aerosol emissions from vegetation fires: particle number and mass emission factors and size distributions, *Atmospheric Chem. Phys.*, 10, 1427–1439, <https://doi.org/10.5194/acp-10-1427-2010>, 2010.

Jen, C. N., Hatch, L. E., Selimovic, V., Yokelson, R. J., Weber, R., Fernandez, A. E., Kreisberg, N. M., Barsanti, K. C., and Goldstein, A. H.: Speciated and total emission factors of particulate organics from burning western US wildland fuels and their dependence on combustion efficiency, *Atmospheric Chem. Phys.*, 19, 1013–1026, <https://doi.org/10.5194/acp-19-1013-2019>, 2019.

Johnston, H. J., Mueller, W., Steinle, S., Vardoulakis, S., Tantrakarnapa, K., Loh, M., and Cherrie, J. W.: How Harmful Is Particulate Matter Emitted from Biomass Burning? A Thailand Perspective, *Curr. Pollut. Rep.*, 5, 353–377, <https://doi.org/10.1007/s40726-019-00125-4>, 2019.

Jolleys, M. D., Coe, H., McFiggans, G., Taylor, J. W., O’Shea, S. J., Le Breton, M., Bauguitte, S. J.-B., Moller, S., Di Carlo, P., Aruffo, E., Palmer, P. I., Lee, J. D., Percival, C. J., and Gallagher, M. W.: Properties and evolution of biomass burning organic aerosol from Canadian boreal forest fires, *Atmospheric Chem. Phys.*, 15, 3077–3095, <https://doi.org/10.5194/acp-15-3077-2015>, 2015.

Junghenn Noyes, K., Kahn, R. A., Limbacher, J. A., Li, Z., Fenn, M. A., Giles, D. M., Hair, J. W., Katich, J. M., Moore, R. H., Robinson, C. E., Sanchez, K. J., Shingler, T. J., Thornhill, K. L., Wiggins, E. B., and Winstead, E. L.: Wildfire Smoke Particle Properties and Evolution, From Space-Based Multi-Angle Imaging II: The Williams Flats Fire during the FIREX-AQ Campaign, *Remote Sens.*, 12, 3823, <https://doi.org/10.3390/rs12223823>, 2020.

Kleinman, L. I., Sedlacek III, A. J., Adachi, K., Buseck, P. R., Collier, S., Dubey, M. K., Hodshire, A. L., Lewis, E., Onasch, T. B., Pierce, J. R., Shilling, J., Springston, S. R., Wang, J., Zhang, Q., Zhou, S., and Yokelson, R. J.: Rapid evolution of aerosol particles and their optical properties downwind of wildfires in the western US, *Atmospheric Chem. Phys.*, 20, 13319–13341, <https://doi.org/10.5194/acp-20-13319-2020>, 2020.

Kodros, J. K., Volckens, J., Jathar, S. H., and Pierce, J. R.: Ambient Particulate Matter Size

Distributions Drive Regional and Global Variability in Particle Deposition in the Respiratory Tract, *GeoHealth*, 2, 298–312, <https://doi.org/10.1029/2018GH000145>, 2018.

Lareau, N. P. and Clements, C. B.: The Mean and Turbulent Properties of a Wildfire Convective Plume, *J. Appl. Meteorol. Climatol.*, 56, 2289–2299, <https://doi.org/10.1175/JAMC-D-16-0384.1>, 2017.

Lee, L. A., Pringle, K. J., Reddington, C. L., Mann, G. W., Stier, P., Spracklen, D. V., Pierce, J. R., and Carslaw, K. S.: The magnitude and causes of uncertainty in global model simulations of cloud condensation nuclei, *Atmospheric Chem. Phys.*, 13, 8879–8914, <https://doi.org/10.5194/acp-13-8879-2013>, 2013.

Leonard, S. S., Castranova, V., Chen, B. T., Schwegler-Berry, D., Hoover, M., Piacitelli, C., and Gaughan, D. M.: Particle size-dependent radical generation from wildland fire smoke, *Toxicology*, 236, 103–113, <https://doi.org/10.1016/j.tox.2007.04.008>, 2007.

Levin, E. J. T., McMeeking, G. R., Carrico, C. M., Mack, L. E., Kreidenweis, S. M., Wold, C. E., Moosmüller, H., Arnott, W. P., Hao, W. M., Collett Jr., J. L., and Malm, W. C.: Biomass burning smoke aerosol properties measured during Fire Laboratory at Missoula Experiments (FLAME), *J. Geophys. Res. Atmospheres*, 115, <https://doi.org/10.1029/2009JD013601>, 2010.

Liu, J. C., Pereira, G., Uhl, S. A., Bravo, M. A., and Bell, M. L.: A systematic review of the physical health impacts from non-occupational exposure to wildfire smoke, *Environ. Res.*, 136, 120–132, <https://doi.org/10.1016/j.envres.2014.10.015>, 2015.

Mardi, A. H., Dadashazar, H., MacDonald, A. B., Braun, R. A., Crosbie, E., Xian, P., Thorsen, T. J., Coggon, M. M., Fenn, M. A., Ferrare, R. A., Hair, J. W., Woods, R. K., Jonsson, H. H., Flagan, R. C., Seinfeld, J. H., and Sorooshian, A.: Biomass Burning Plumes in the Vicinity of the California Coast: Airborne Characterization of Physicochemical Properties, Heating Rates, and Spatiotemporal Features, *J. Geophys. Res. Atmospheres*, 123, 13,560–13,582, <https://doi.org/10.1029/2018JD029134>, 2018.

May, A. A., Levin, E. J. T., Hennigan, C. J., Riipinen, I., Lee, T., Collett Jr., J. L., Jimenez, J. L., Kreidenweis, S. M., and Robinson, A. L.: Gas-particle partitioning of primary organic aerosol emissions: 3. Biomass burning, *J. Geophys. Res. Atmospheres*, 118, 11,327–11,338, <https://doi.org/10.1002/jgrd.50828>, 2013.

May, A. A., Lee, T., McMeeking, G. R., Akagi, S., Sullivan, A. P., Urbanski, S., Yokelson, R. J., and Kreidenweis, S. M.: Observations and analysis of organic aerosol evolution in some prescribed fire smoke plumes, *Atmospheric Chem. Phys.*, 15, 6323–6335, <https://doi.org/10.5194/acp-15-6323-2015>, 2015.

O'Dell, K., Ford, B., Fischer, E. V., and Pierce, J. R.: Contribution of Wildland-Fire Smoke to US PM_{2.5} and Its Influence on Recent Trends, *Environ. Sci. Technol.*, 53, 1797–1804, <https://doi.org/10.1021/acs.est.8b05430>, 2019.

Palm, B. B., Peng, Q., Fredrickson, C. D., Lee, B. H., Garofalo, L. A., Pothier, M. A., Kreidenweis, S. M., Farmer, D. K., Pokhrel, R. P., Shen, Y., Murphy, S. M., Permar, W., Hu, L., Campos, T. L., Hall, S. R., Ullmann, K., Zhang, X., Flocke, F., Fischer, E. V., and Thornton, J. A.: Quantification of organic aerosol and brown carbon evolution in fresh wildfire plumes, *Proc. Natl. Acad. Sci.*, 117, 29469–29477, <https://doi.org/10.1073/pnas.2012218117>, 2020.

Peng, Q., Palm, B. B., Melander, K. E., Lee, B. H., Hall, S. R., Ullmann, K., Campos, T., Weinheimer, A. J., Apel, E. C., Hornbrook, R. S., Hills, A. J., Montzka, D. D., Flocke, F., Hu, L., Permar, W., Wielgasz, C., Lindaas, J., Pollack, I. B., Fischer, E. V., Bertram, T. H., and Thornton, J. A.: HONO Emissions from Western U.S. Wildfires Provide Dominant Radical Source in Fresh Wildfire Smoke, *Environ. Sci. Technol.*, 54, 5954–5963, <https://doi.org/10.1021/acs.est.0c00126>, 2020.

Petters, M. D. and Kreidenweis, S. M.: A single parameter representation of hygroscopic growth and cloud condensation nucleus activity, *Atmospheric Chem. Phys.*, 7, 1961–1971, <https://doi.org/10.5194/acp-7-1961-2007>, 2007.

Petters, M. D., Carrico, C. M., Kreidenweis, S. M., Prenni, A. J., DeMott, P. J., Collett Jr., J. L., and Moosmüller, H.: Cloud condensation nucleation activity of biomass burning aerosol, *J. Geophys. Res. Atmospheres*, 114, <https://doi.org/10.1029/2009JD012353>, 2009.

Pierce, J. R. and Adams, P. J.: Efficiency of cloud condensation nuclei formation from ultrafine particles, *Atmospheric Chem. Phys.*, 7, 1367–1379, <https://doi.org/10.5194/acp-7-1367-2007>, 2007.

Ramnarine, E., Kodros, J. K., Hodshire, A. L., Lonsdale, C. R., Alvarado, M. J., and Pierce, J. R.: Effects of near-source coagulation of biomass burning aerosols on global predictions of aerosol size distributions and implications for aerosol radiative effects, *Atmospheric Chem. Phys.*, 19, 6561–6577, <https://doi.org/10.5194/acp-19-6561-2019>, 2019.

Reid, C. E., Brauer, M., Johnston, F. H., Jerrett, M., Balme, J. R., and Elliott, C. T.: Critical Review of Health Impacts of Wildfire Smoke Exposure, *Environ. Health Perspect.*, 124, 1334–1343, <https://doi.org/10.1289/ehp.1409277>, 2016.

Reid, J. S., Hobbs, P. V., Ferek, R. J., Blake, D. R., Martins, J. V., Dunlap, M. R., and Liousse, C.: Physical, chemical, and optical properties of regional hazes dominated by smoke in Brazil, *J. Geophys. Res. Atmospheres*, 103, 32059–32080, <https://doi.org/10.1029/98JD00458>, 1998.

Reid, J. S., Koppmann, R., Eck, T. F., and Eleuterio, D. P.: A review of biomass burning emissions part II: intensive physical properties of biomass burning particles, *Atmos Chem Phys*, 27, 2005.

Riipinen, I., Pierce, J. R., Yli-Juuti, T., Nieminen, T., Häkkinen, S., Ehn, M., Junninen, H., Lehtipalo, K., Petäjä, T., Slowik, J., Chang, R., Shantz, N. C., Abbatt, J., Leaitch, W. R., Kerminen, V.-M., Worsnop, D. R., Pandis, S. N., Donahue, N. M., and Kulmala, M.: Organic condensation: a vital link connecting aerosol formation to cloud condensation nuclei (CCN) concentrations, *Atmospheric Chem. Phys.*, 11, 3865–3878,

<https://doi.org/10.5194/acp-11-3865-2011>, 2011.

Sakamoto, K. M., Allan, J. D., Coe, H., Taylor, J. W., Duck, T. J., and Pierce, J. R.: Aged boreal biomass-burning aerosol size distributions from BORTAS 2011, *Atmospheric Chem. Phys.*, 15, 1633–1646, <https://doi.org/10.5194/acp-15-1633-2015>, 2015.

Sakamoto, K. M., Laing, J. R., Stevens, R. G., Jaffe, D. A., and Pierce, J. R.: The evolution of biomass-burning aerosol size distributions due to coagulation: dependence on fire and meteorological details and parameterization, *Atmospheric Chem. Phys.*, 16, 7709–7724, <https://doi.org/10.5194/acp-16-7709-2016>, 2016.

Seinfeld, J. H. and Pandis, S. N.: *Atmospheric Chemistry and Physics: From Air Pollution to Climate Change*, John Wiley & Sons, Incorporated, New York, UNITED STATES, 2016.

Shrivastava, M., Cappa, C. D., Fan, J., Goldstein, A. H., Guenther, A. B., Jimenez, J. L., Kuang, C., Laskin, A., Martin, S. T., Ng, N. L., Petaja, T., Pierce, J. R., Rasch, P. J., Roldin, P., Seinfeld, J. H., Shilling, J., Smith, J. N., Thornton, J. A., Volkamer, R., Wang, J., Worsnop, D. R., Zaveri, R. A., Zelenyuk, A., and Zhang, Q.: Recent advances in understanding secondary organic aerosol: Implications for global climate forcing, *Rev. Geophys.*, 55, 509–559, <https://doi.org/10.1002/2016RG000540>, 2017.

Spracklen, D. V., Carslaw, K. S., Pöschl, U., Rap, A., and Forster, P. M.: Global cloud condensation nuclei influenced by carbonaceous combustion aerosol, *Atmospheric Chem. Phys.*, 11, 9067–9087, <https://doi.org/10.5194/acp-11-9067-2011>, 2011.

Twomey, S.: Pollution and the planetary albedo, *Atmospheric Environ.* 1967, 8, 1251–1256, [https://doi.org/10.1016/0004-6981\(74\)90004-3](https://doi.org/10.1016/0004-6981(74)90004-3), 1974.

Vakkari, V., Kerminen, V.-M., Beukes, J. P., Tiitta, P., van Zyl, P. G., Josipovic, M., Venter, A. D., Jaars, K., Worsnop, D. R., Kulmala, M., and Laakso, L.: Rapid changes in biomass burning aerosols by atmospheric oxidation, *Geophys. Res. Lett.*, 41, 2644–2651, <https://doi.org/10.1002/2014GL059396>, 2014.

Wang, S., Coggon, M. M., Gkatzelis, G. I., Warneke, C., Bourgeois, I., Ryerson, T., Peischl, J., Veres, P. R., Neuman, J. A., Hair, J., Shingler, T., Fenn, M., Diskin, G., Huey, L. G., Lee, Y. R., Apel, E. C., Hornbrook, R. S., Hills, A. J., Hall, S. R., Ullmann, K., Bela, M. M., Trainer, M. K., Kumar, R., Orlando, J. J., Flocke, F. M., and Emmons, L. K.: Chemical Tomography in a Fresh Wildland Fire Plume: A Large Eddy Simulation (LES) Study, *J. Geophys. Res. Atmospheres*, 126, e2021JD035203, <https://doi.org/10.1029/2021JD035203>, 2021.

Yokelson, R. J., Crouse, J. D., DeCarlo, P. F., Karl, T., Urbanski, S., Atlas, E., Campos, T., Shinozuka, Y., Kapustin, V., Clarke, A. D., Weinheimer, A., Knapp, D. J., Montzka, D. D., Holloway, J., Weibring, P., Flocke, F., Zheng, W., Toohey, D., Wennberg, P. O., Wiedinmyer, C., Mauldin, L., Fried, A., Richter, D., Walega, J., Jimenez, J. L., Adachi, K., Buseck, P. R., Hall, S. R., and Shetter, R.: Emissions from biomass burning in the Yucatan, *Atmospheric Chem. Phys.*, 9, 5785–5812, <https://doi.org/10.5194/acp-9-5785-2009>, 2009.

Zhang, X., Pandis, S. N., and Seinfeld, J. H.: Diffusion-Limited Versus Quasi-Equilibrium Aerosol Growth, *Aerosol Sci. Technol.*, 46, 874–885, <https://doi.org/10.1080/02786826.2012.679344>, 2012.

Zhou, S., Collier, S., Jaffe, D. A., Briggs, N. L., Hee, J., Sedlacek III, A. J., Kleinman, L., Onasch, T. B., and Zhang, Q.: Regional influence of wildfires on aerosol chemistry in the western US and insights into atmospheric aging of biomass burning organic aerosol, *Atmospheric Chem. Phys.*, 17, 2477–2493, <https://doi.org/10.5194/acp-17-2477-2017>, 2017.

Appendices

Appendix A: Supplementary Tables

Table A.1: Relationship between σ_θ and σ_ϕ and stability class. Where $\sigma_\theta = \frac{\sigma_v}{u}$ and $\sigma_\phi = \frac{\sigma_w}{u}$

Source: (Arya, 1999)

Stability Class	σ_θ [deg.]	σ_ϕ [deg.]
A	≥ 22.5	≥ 11.5
B	17.5 - 22.5	10.0 - 11.5
C	12.5 - 17.5	7.8 - 10.0
D	7.5 - 12.5	5.0 - 7.8
E	3.8 - 7.5	2.4 - 5.0
F	< 3.8	< 2.4

Table A.2: The age of the youngest sampled transect, the selected transect used for initializing the simulations in our study, and the reason for modification for each of the eight samplings.

Sampling	Sampled Youngest Age [s]	Selected Initialization Age [s]	Reason
7/25	886.733	2709.930	First 5 sampled transects had a linear decrease in $\ln(\Delta\text{CO})$ (7.7 to 6.4), then increased to 8.1 before starting to linearly decrease again. More transects follow the trend that began with $\ln(\Delta\text{CO}) = 8.1$, so this is selected.
7/29	305.798	999.268	No decrease in $\ln(\Delta\text{CO})$ between these two transects (5.3) and at a different altitude (3800 m and 4500 m)
8/3 P1	398.612	2916.29	Using Lagrangian transects following Wang et al. (2021)
8/3 P2	707.126	2990.55	Youngest sampled age had a lower $\ln(\Delta\text{CO})$ at 7.7 than the second sampled (selected initialization transect) at 7.9
8/6	329.406	329.406	Removed the second sampled transect due to its $\ln(\Delta\text{CO})$ being higher than the others and not following a similar rate of decay.
8/7 P1	2471.98	2471.98	No change
8/7 P2	1904.55	3442.37	$\ln(\Delta\text{CO})$ of the youngest sampled was the lowest of all other transects sampled in this pass
8/12	2691.49	2809.77	Similar age and $\ln(\Delta\text{CO})$ for these two. Differed in diameter (140 nm and 150 nm) and in number concentration (16000 cm^{-3} and 58000 cm^{-3})

Appendix B: Supplementary Figures

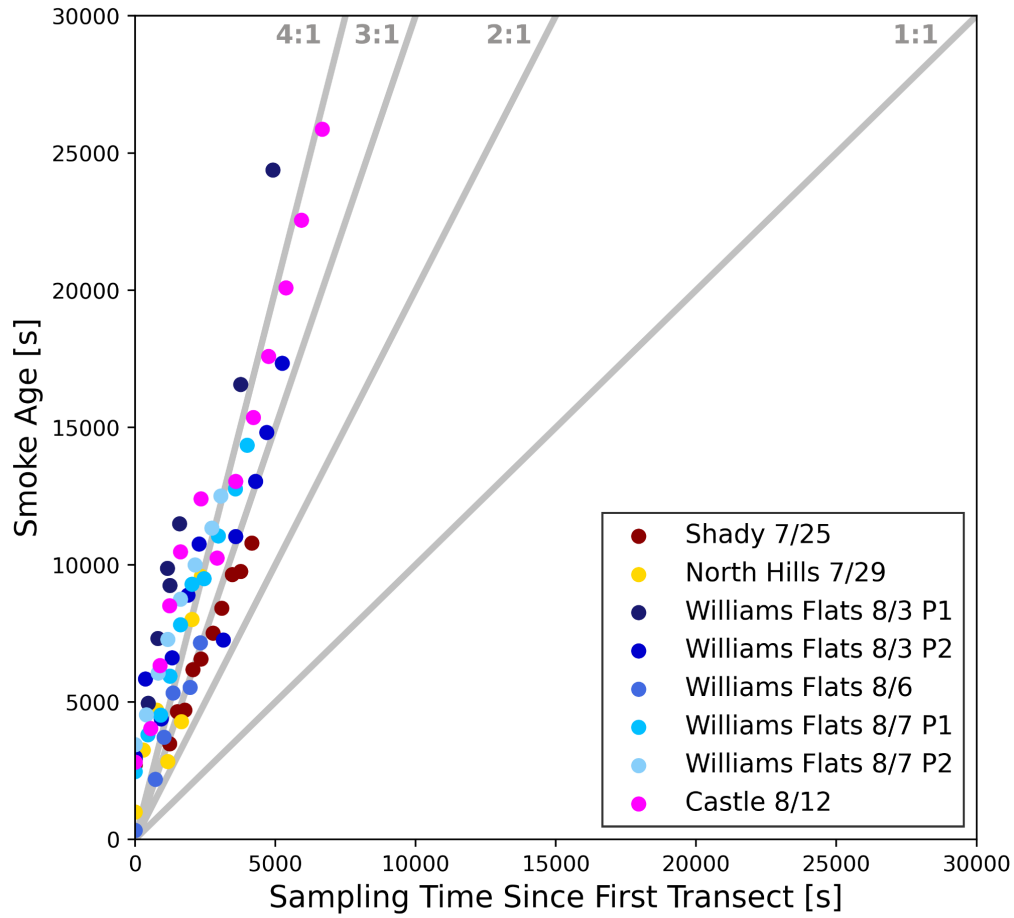


Figure A.1: The physical smoke age versus the sampling time since the first transect in seconds for each of the eight sets of transects. The gray lines have slopes of 4, 3, 2 and 1, with the 1:1 line representing the ideal slope for Lagrangian sampling.

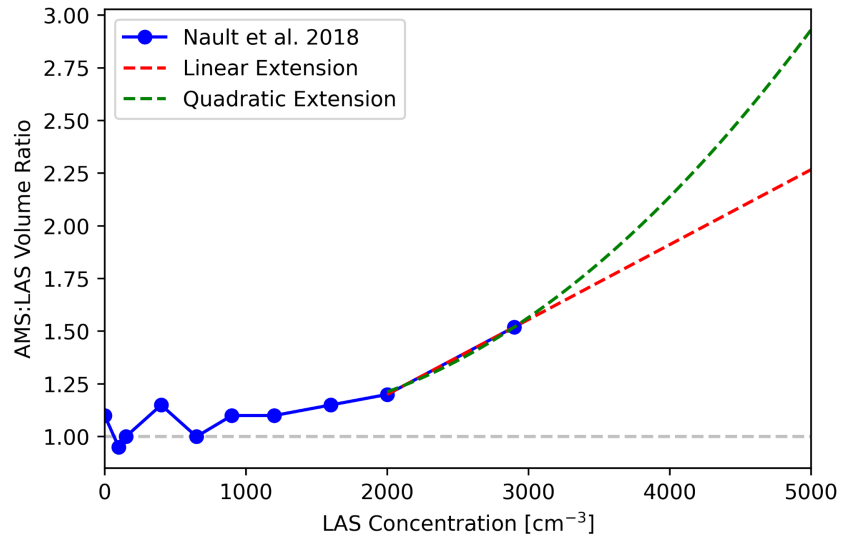


Figure A.2: The AMS:LAS volume ratios versus LAS concentration used to saturation correct the LAS measurements. Below the LAS measurements of 2000 cm⁻³ with the impact of the dilution system of the instrument removed, results from Nault et al. 2018 (blue) are used to correct saturation. Above 2000 cm⁻³, the linear extension (red dashed line) is used to saturation correct measurements at higher concentrations. Due to the uncertainty of what this function should be, correcting these higher concentrations with a quadratic extension (green dashed line) is also examined.

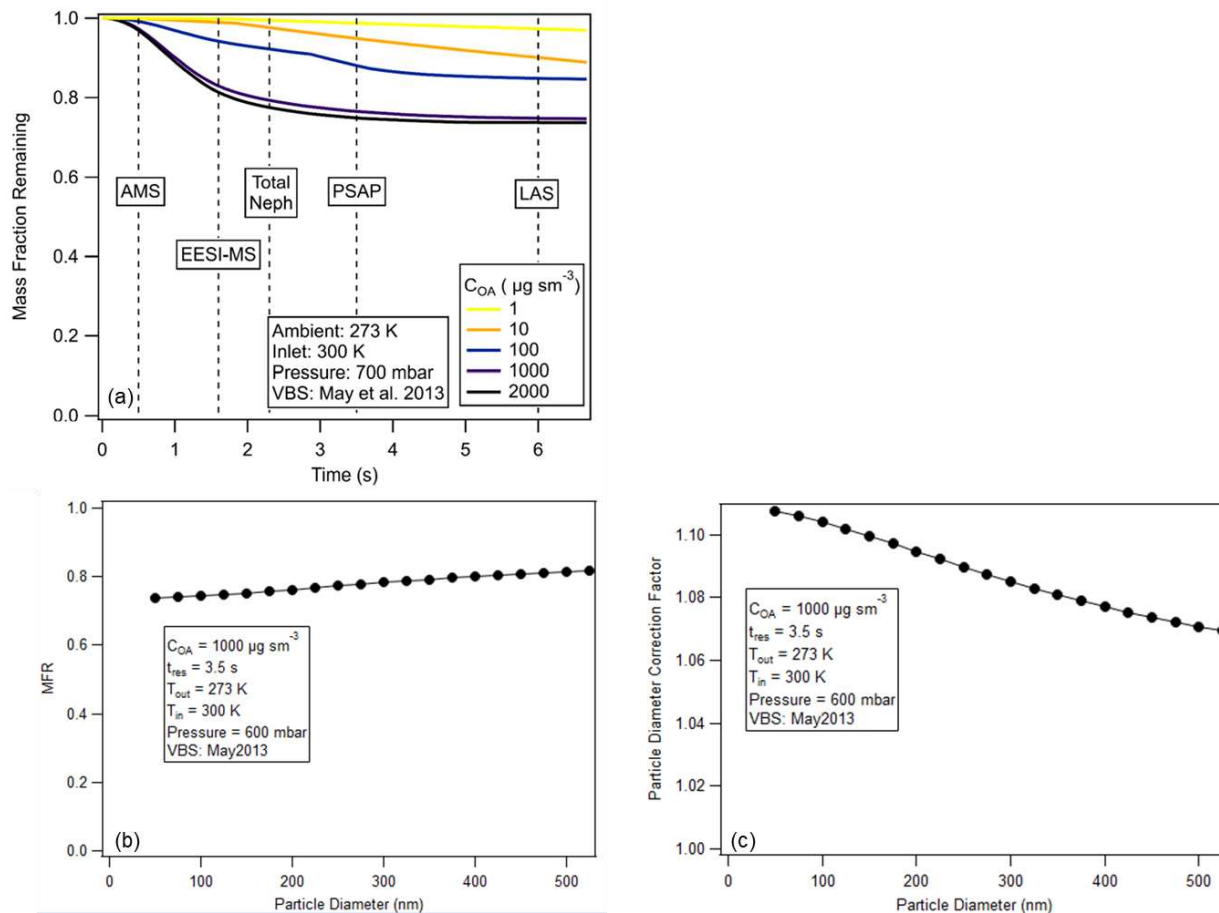


Figure A.3: (a) The mass fraction remaining at each instrument for various concentrations of OA assuming a diameter of 300 nm, an ambient temperature of 273 K, and an inlet temperature of 300 K (Pagonis et al., 2021). (b) An example of the size dependency of the mass fraction remaining (MFR), and (c) the correction factor for the particle diameter for an OA concentration of $1000 \mu\text{g m}^{-3}$, an ambient temperature of 273 K, and an inlet temperature of 300 K.

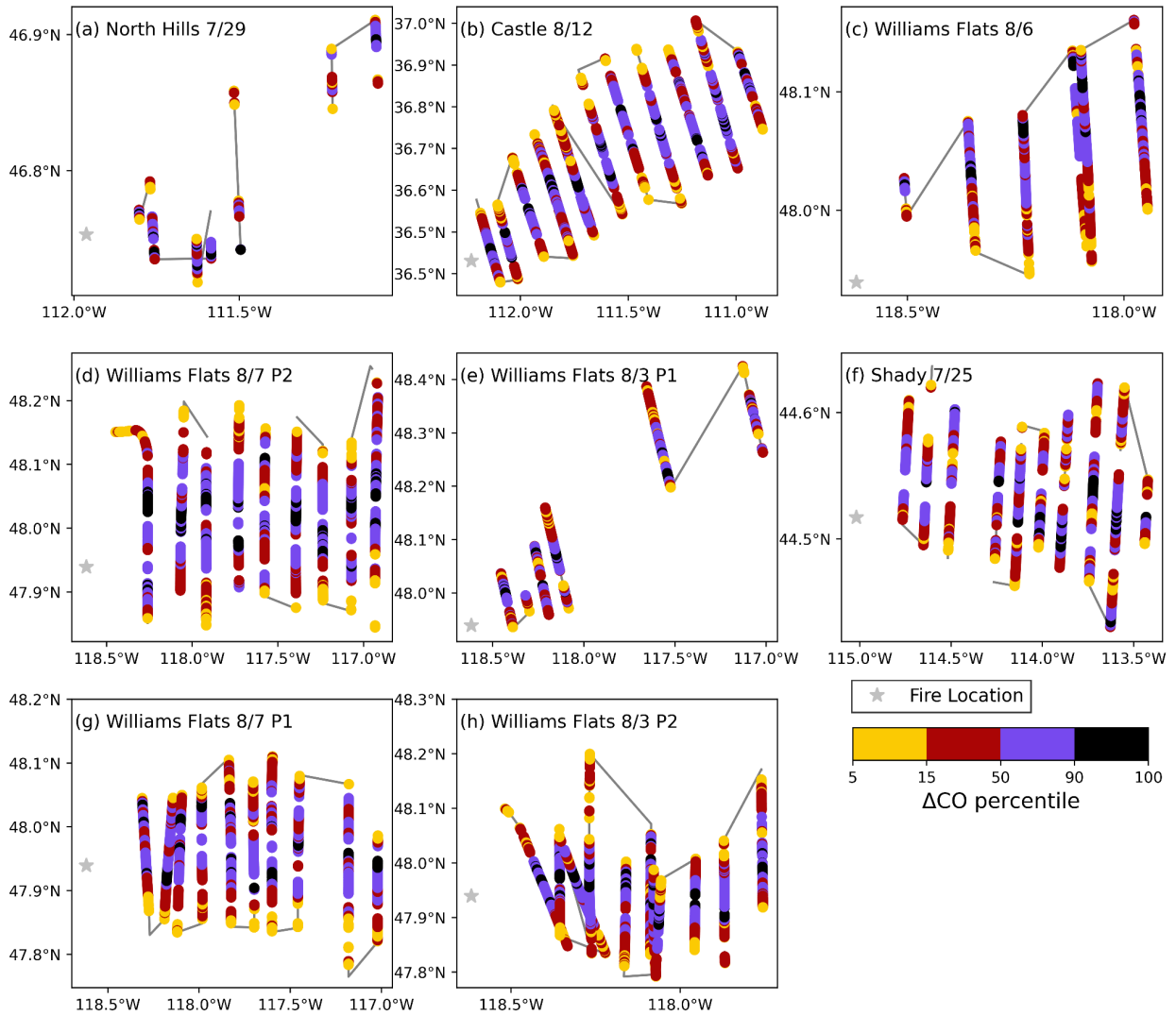


Figure A.4: Flight tracks used in this study, with the location of the fire ignition shown as well. This location is not necessarily indicative of the location of fire emissions at the time of the DC8 sampling. The coloring is by ΔCO percentile, noting that the size of these percentile bins varies.

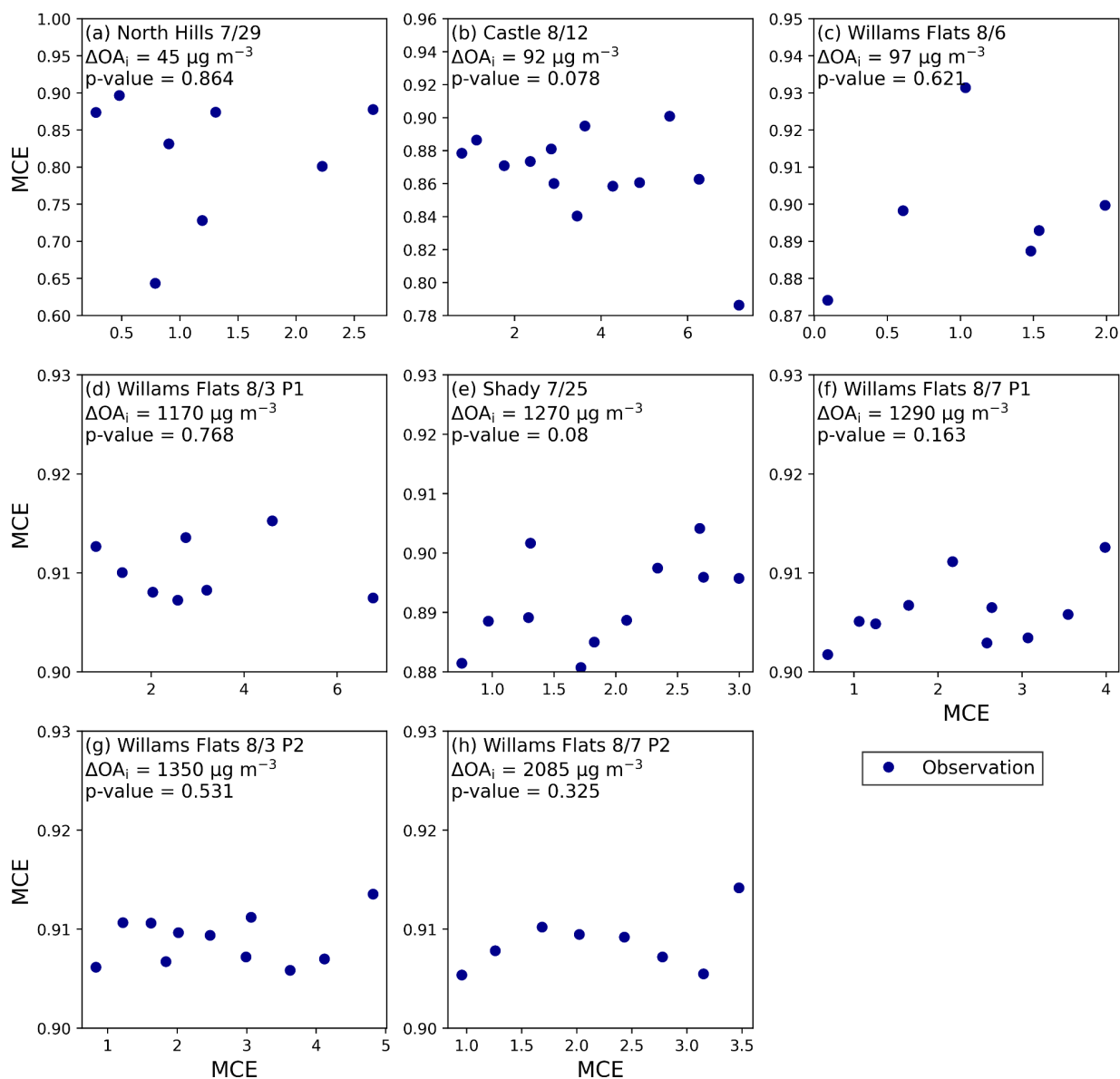


Figure A.5: The modified combustion efficiency (MCE) versus smoke age for each of the eight flights, organized so that (a)-(h) are in order of increasing ΔOA_i . The in-plot text shows the ΔOA_i and the p-value of the linear regression of MCE with smoke age.

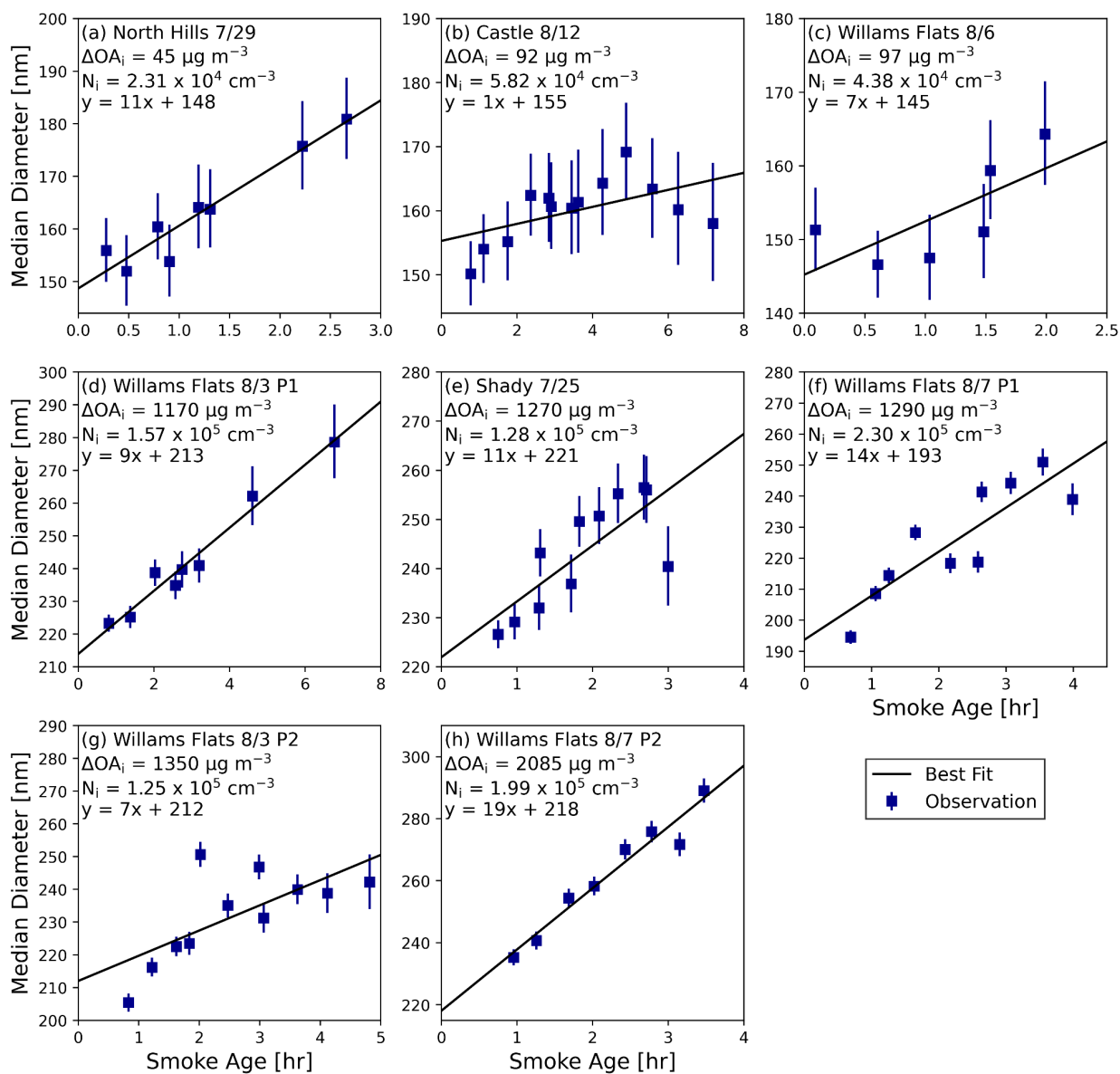


Figure A.6: The median diameter (D_p) versus smoke age for each of the eight flights, organized so that (a)-(h) are in order of increasing ΔOA_i . The error bars represent the standard deviation of D_p within the transect.

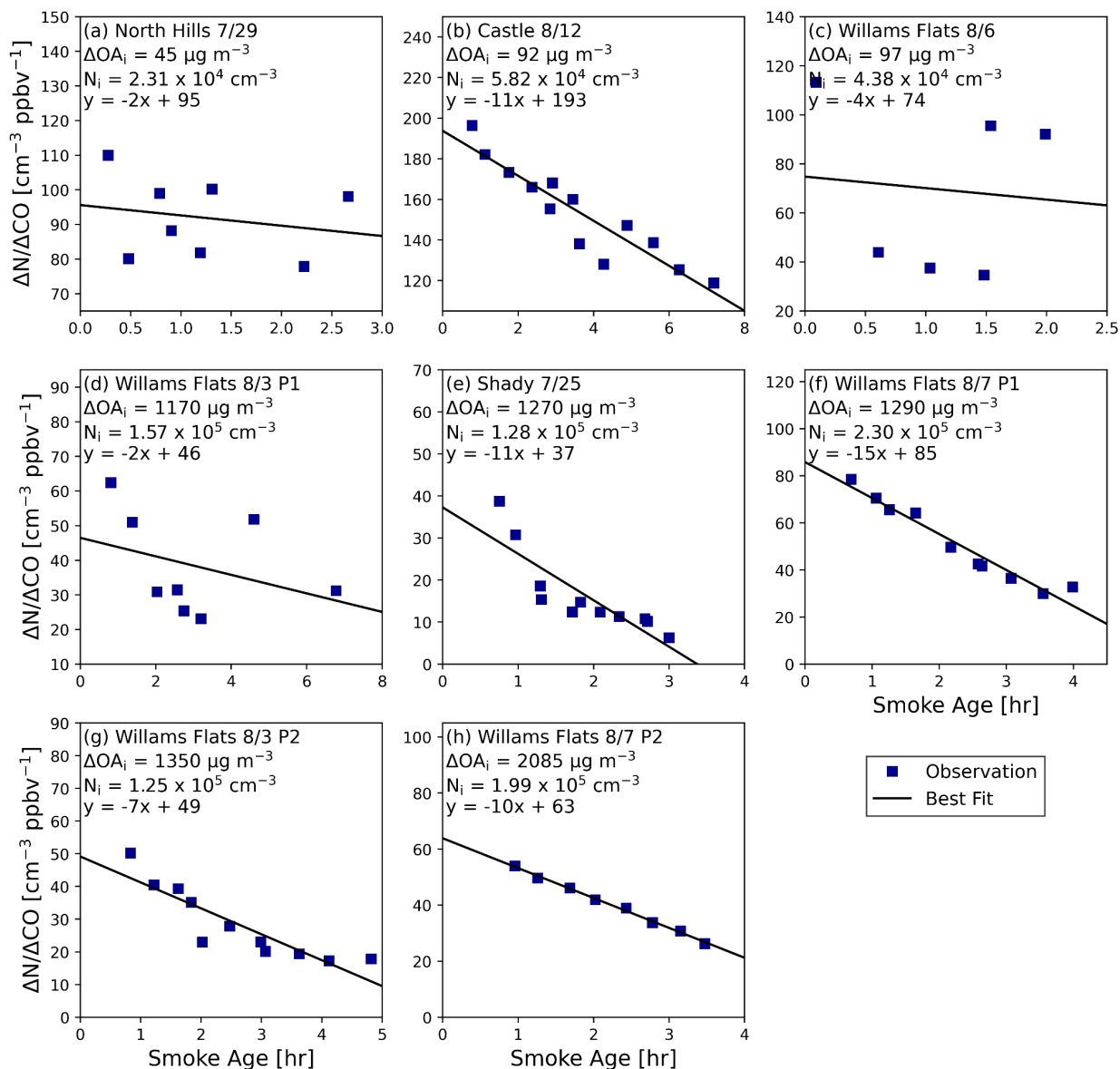


Figure A.7: The number enhancement ratio ($\Delta N/\Delta CO$) versus smoke age for each of the eight flights, organized so that (a)-(h) are in order of increasing ΔOA_i .

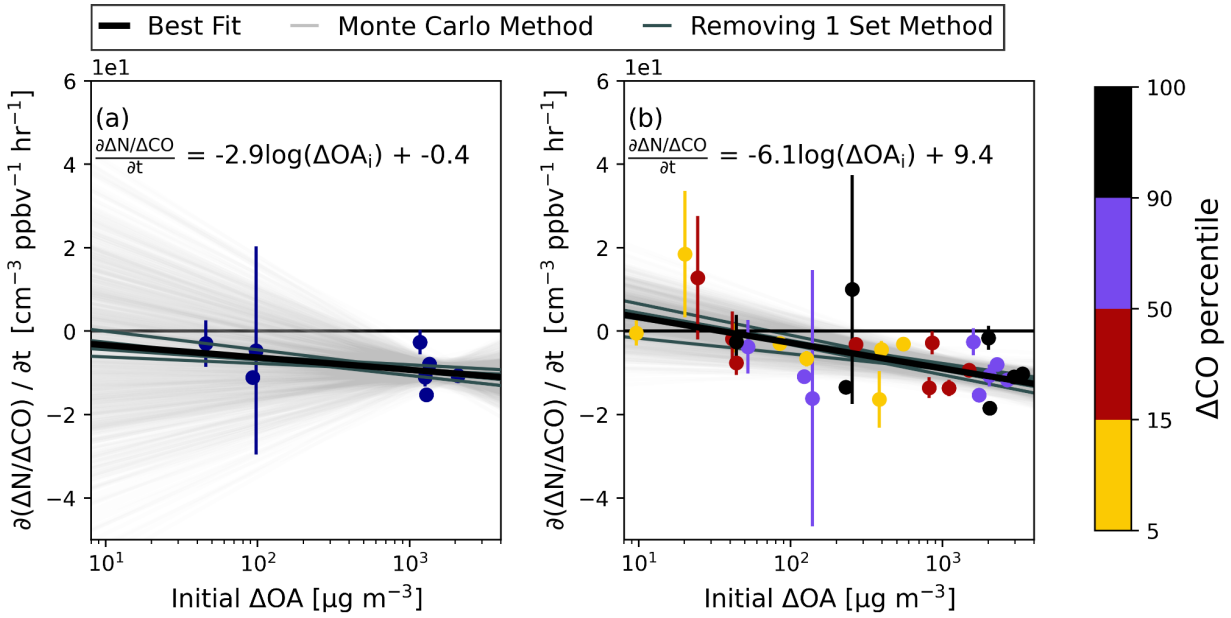


Figure A.8: Observed slopes of $\Delta N/\Delta CO$ with smoke age based on ordinary least squares linear regressions as a function of ΔOA_i for (a) the transect averages and (b) by ΔCO percentile for each set of transects.. The error bars indicate the 95% confidence interval for the $\Delta N/\Delta CO$ slope. 1000 best fit lines from a Monte Carlo technique are shown in light gray. The darker gray lines are the results of linear regressions with one sample removed. The solid black line is the linear regression for the points at the center of the error bars; the equation for this line is shown on each panel.

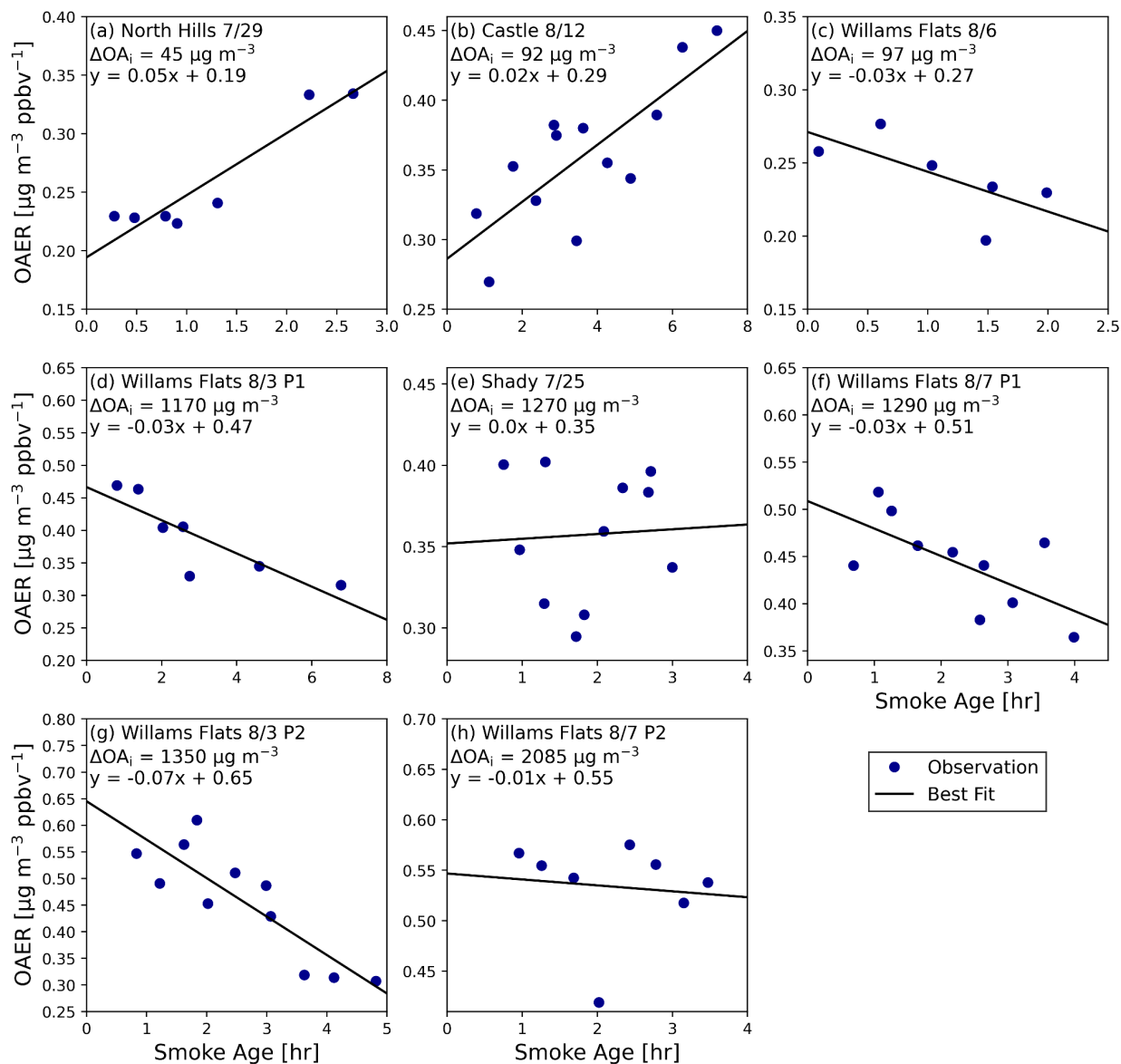


Figure A.9: The organic aerosol excess mixing ratio (OAER) versus smoke age for each of the eight flights, organized so that (a)-(h) are in order of increasing ΔOA_i .

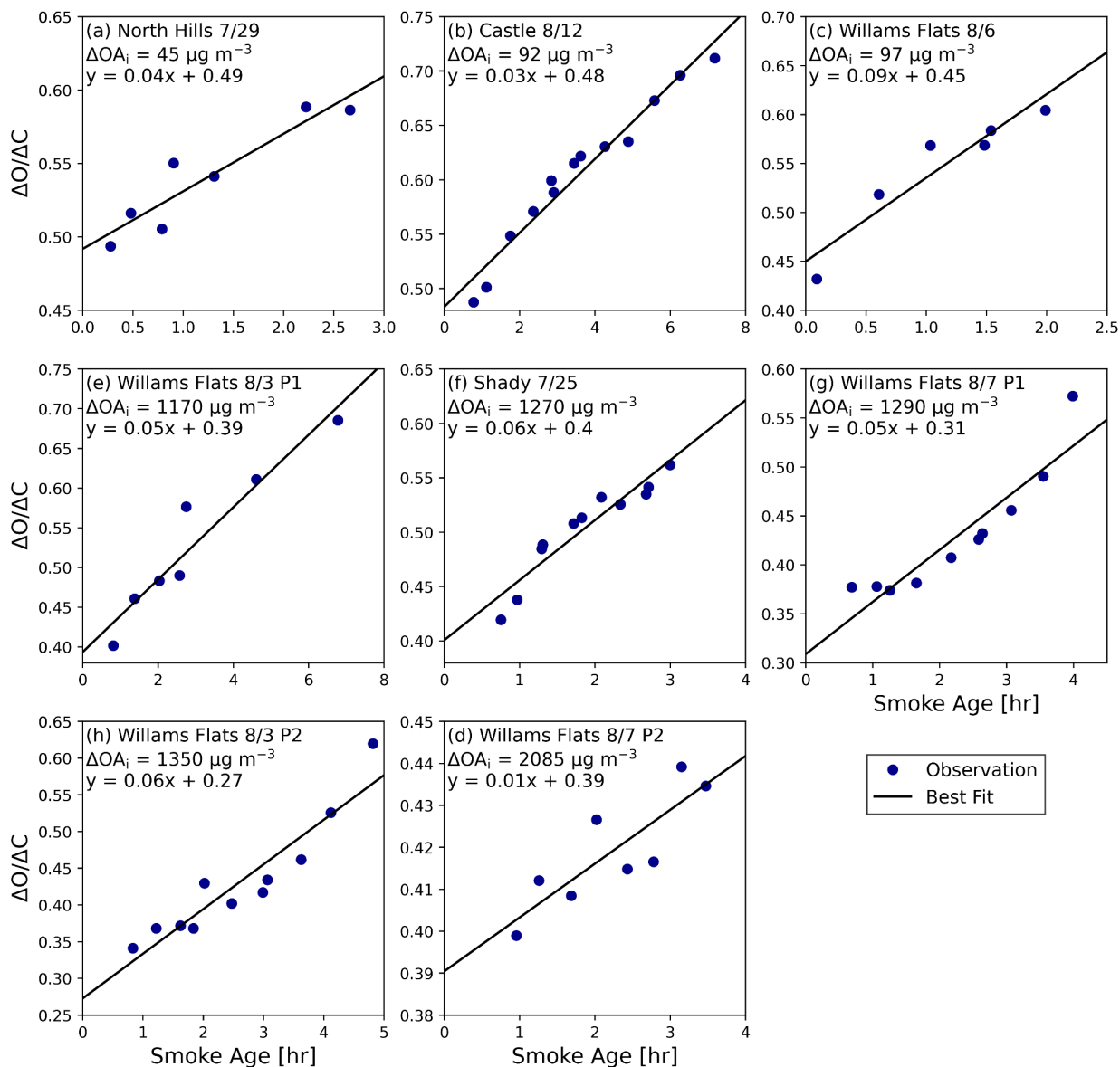


Figure A.10: The $\Delta O:\Delta C$ versus smoke age for each of the eight flights, organized so that (a)-(h) are in order of increasing ΔOA_i .

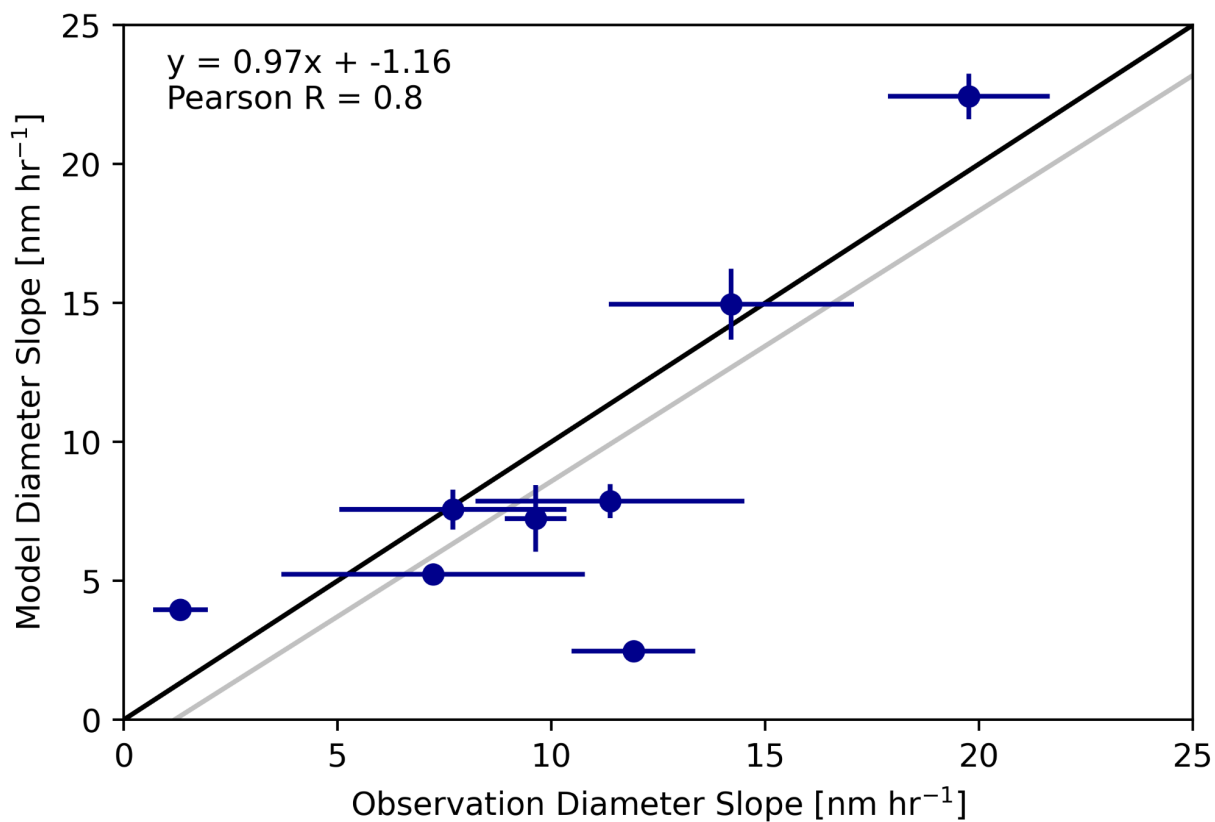


Figure A.11: The modeled rate of change of median diameter with smoke age versus the observed rate of change of median diameter with smoke age. The error bars represent the respective 95% confidence intervals of the rates of change. The black line is the 1:1 line, and the gray line is the linear regression.

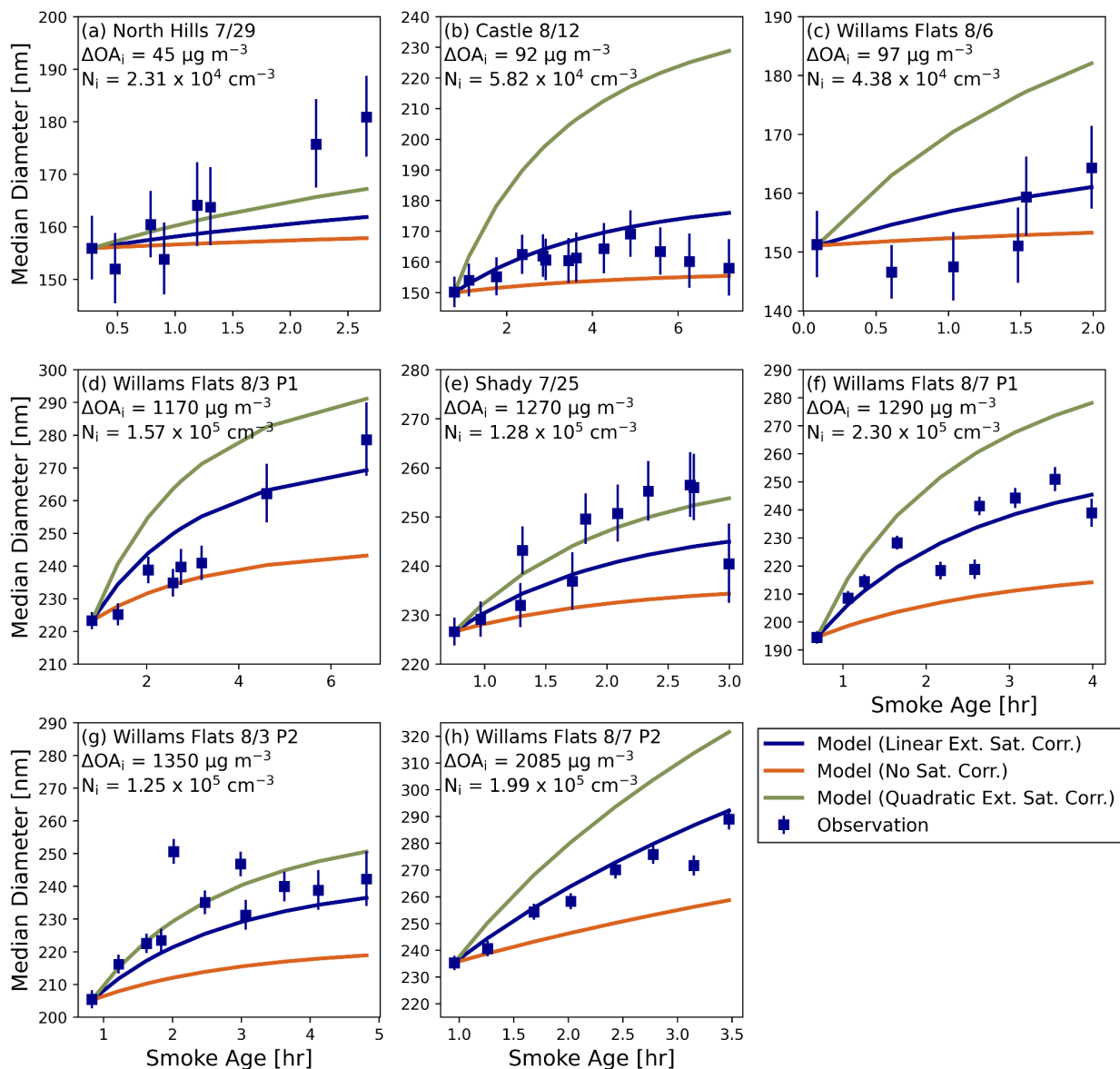


Figure A.12: The transect averaged observed median diameter, along with the simulated median diameter with coagulation and dilution based on either no saturation correction (orange), a linear extended saturation correction (blue), or a quadratic extended saturation correction (green). The error bars represent the standard deviation of D_p within the transect. (a) to (h) are organized in order of increasing ΔOA_i .

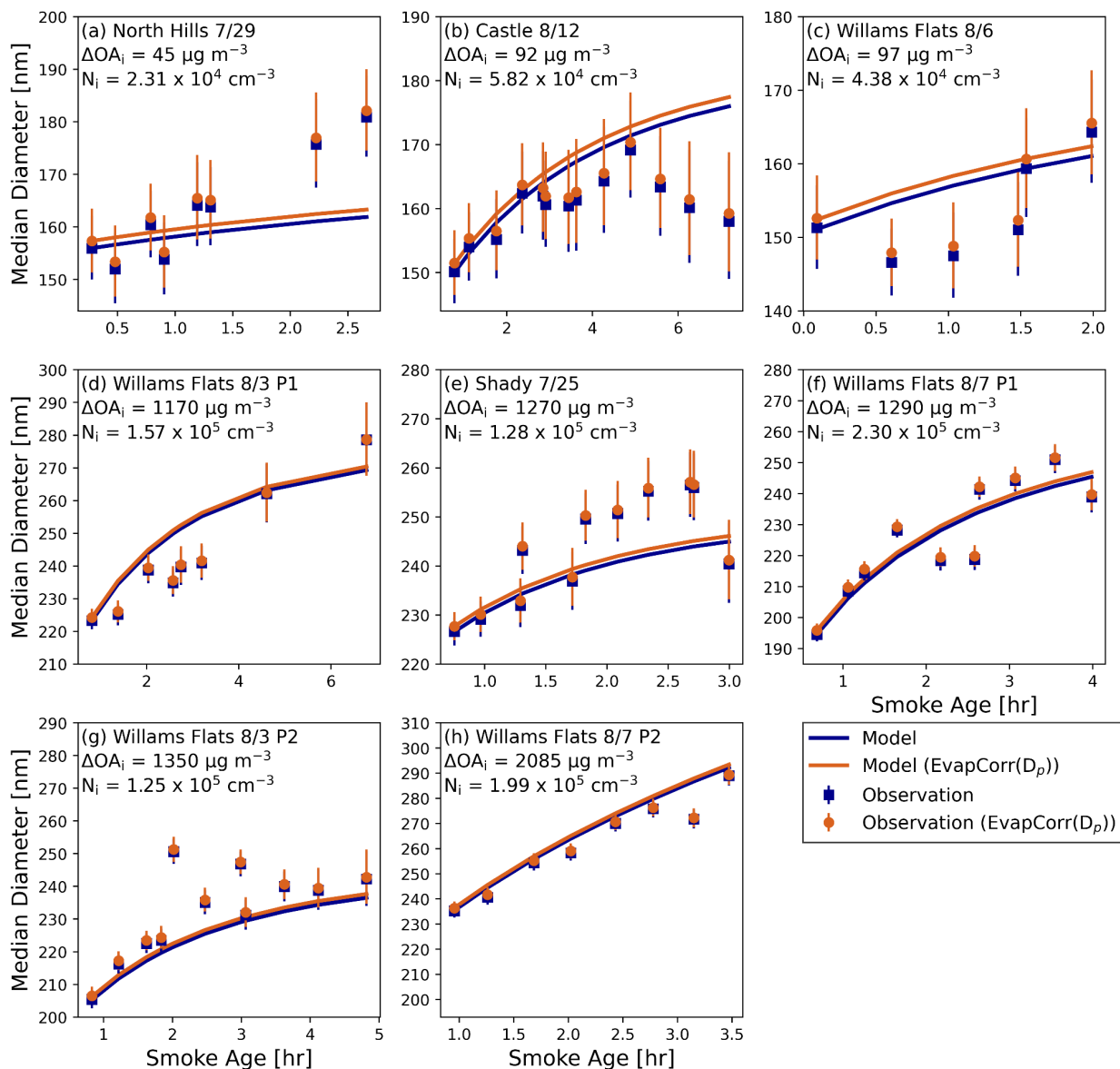


Figure A.13: The observed and coagulation simulated transect averaged median diameter as a function of smoke age with the LAS evaporation correction having no size dependency (blue), and with the evaporation correction for the LAS having a size dependency (orange). The error bars represent the standard deviation of D_p within the transect. (a) to (h) are organized in order of increasing ΔOA_i .

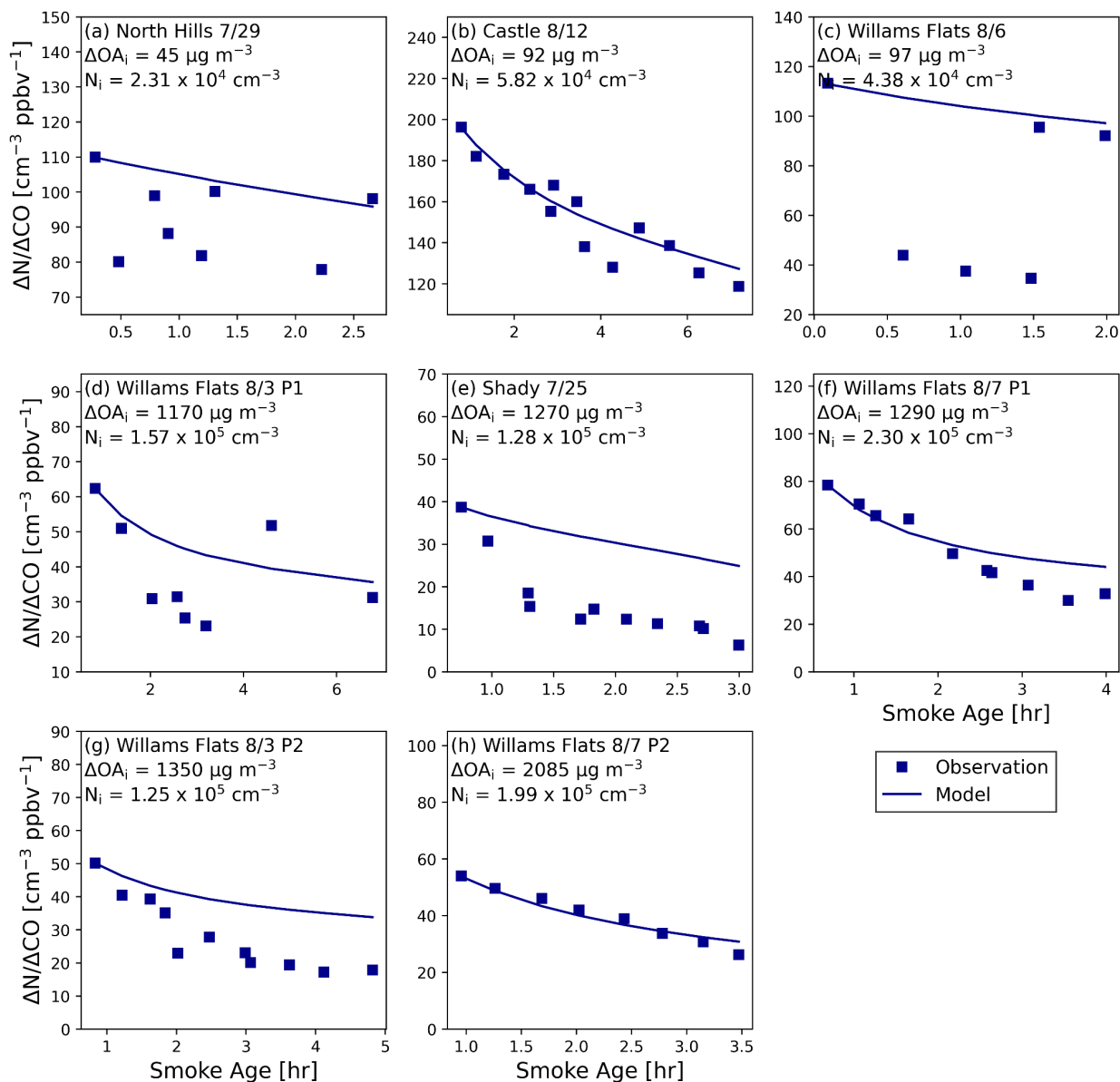


Figure A.14: The observed and simulated number enhancement ratio ($\Delta N/\Delta CO$) with smoke age for each of the eight sets of transects, with (a) to (h) organized in order of increasing ΔOA_i .